# Speed-Sensorless Control of Linear Induction Motor Based on the SSLKF-PLL Speed Estimation Scheme

Wang, Huimin; Yang, Yongheng; Ge, Xinglai; Li, Songtao; Zuo, Yun

*Published in:*
I E E E Transactions on Industry Applications

*DOI (link to publication from Publisher):*
10.1109/TIA.2020.3008673

*Publication date:*
2020

*Document Version*
Accepted author manuscript, peer reviewed version

# Speed-Sensorless Control of Linear Induction Motor Based on the SSLKF-PLL Speed Estimation Scheme

Huimin Wang, *Student Member*, *IEEE*, Yongheng Yang, *Senior Member*, *IEEE*, Xinglai Ge, *Member*, *IEEE*, Songtao Li, and Yun Zuo

***Abstract* – In most motor drive applications, the speed sensor is of concern because it potentially deteriorates the system reliability and increases the system cost. To mitigate the adverse effects from speed sensors, various speed estimation schemes are employed to achieve speed-sensorless control of motor drives. With this, the concept of the steady-state linear Kalman filter-based phase-locked loop (SSLKF-PLL) is adopted in this paper to enable speed estimation for speed-sensorless control of linear induction motor (LIM) drives. However, the SSLKF-PLL scheme may be challenged by disturbances, e.g., harmonics and parameter variations in practice. To address this issue, the disturbance rejection schemes, including the pre-filters and amplitude normalization unit, are developed for the SSLKF-PLL scheme in this paper. Additionally, the dynamic performance analysis and parameter tuning of the SSLKF-PLL scheme are detailed by using the derived small signal model. Experimental tests have validated the analysis and discussions of the SSLKF-PLL scheme.**

***Index Terms*—Motor drive, speed estimation, pre-filter, amplitude normalization, dynamic analysis, steady-state linear Kalman filter-based phase locked-loop (SSLKF-PLL)**

## I. INTRODUCTION

INCRESING demands to mitigate traffic congestion call for the new-generation rail transit systems. The medium-low speed maglev, driven by linear induction motor (LIM), is a promising candidate for next-generation rail systems. Key characteristics of the medium-low speed maglev include small turning radius, low maintenance cost and friendly-environment effect [1]-[3]. One of the major concerns in the LIM drives is the requirement of speed sensors, which may contribute to the reduced system reliability and increased system cost. Consequently, many attempts have been made in the literature to properly estimate the motor speed, and then, speed sensors can be removed [4].

Manuscript received October 26, 2019; revised December 26, 2019, March 11, 2020 and May 20, 2020; accepted June 28, 2020. This work was supported by the High-Speed Railway Joint Funds of the National Natural Science Foundation of China (U1934204), and the Doctoral Innovation Fund Program of Southwest Jiaotong University under Grant D-CX201916. (*Corresponding author: Xinglai Ge*.).

H. Wang, X. Ge, S. Li and Y. Zuo are with the Ministry of Education Key Laboratory of Magnetic Suspension Technology and Maglev Vehicle, Southwest Jiaotong University, Chengdu 610031, China (e-mail: wanghuimin@my.swjtu.edu.cn;xlgee@163.com;SongtaoLi@my.swjtu.edu.cn; z _uoy_un@163.com).

Y. Yang is with the Department of Energy Technology, Aalborg University, Aalborg 9220, Denmark (e-mail: yoy@et.aau.dk)

Speed estimation schemes based on the motor model attract much popularity in the speed-sensorless control of LIM drives. The limitation is that the special structure of the LIM makes the speed estimation schemes using the concept of the non-ideal phenomena behave unsatisfactorily. In contrast, the model-based speed estimation schemes can provide easier implementation and more adjustment flexibility, compared to the non-ideal-phenomena-based speed estimation schemes, although the thorny issue of parameter variations should be tackled well. The reported model-based speed estimation schemes for speed-sensorless control of LIM drives include the model reference adaptive system (MRAS) [5], the adaptive full-order observer [6], the Kalman filter [7], the closed-loop observer [8] and the second-order sliding mode observer [9]. Another possibility to achieve acceptable speed estimation is the use of advanced control methods, e.g., the fuzzy control [10], [11] and the nonlinear predictive control [12].

For synchronization in power electronics and power systems applications, the phase-locked loop (PLL) technique is attractive due to its satisfactory estimation and simple structure [13]-[15]. Accordingly, explorations on the PLL have been extended to the sensorless control of motor drives, especially the sensorless control of permanent-magnet synchronous motor (PMSM) drives [16]-[21]. The PLL-based estimation schemes with various filters have been proven as an effective method for speed or phase estimation of sesnorless control of interior PMSM (IPMSM) drives. Filters like the recursive-least-square-based adaptive filter (RLS-AF) [18], the adaptive notch filter (ANF) [19], the adaptive linear neural (ADALINE)-network-based filter [20] and the multiple adaptive vector filter (MAVF) [21] can be adopted. Furthermore, a PLL-based speed estimation scheme for sensorless control of surface-mounted permanent magnet synchronous generator (SPMSG) drives was proposed in [22]. The main feature of this scheme was to employ a novel finite position set phase-locked loop (FPS-PLL) for performance improvement. Another PLL-type speed estimation scheme for three-phase machines was presented in [23], where the stability analysis along with the parameter design was performed by using the linearized model of this scheme. In addition, a vector-PLL-based scheme that accomplished the rotor position estimation and the rotor speed estimation simultaneously, was presented in [24] for sensorless control of doubly-fed induction motor (DFIM) drives, and the stability analysis of this PLL-based estimator was also made.

In general, a proportional-integral (PI) controller, acting as the loop filter (LF), is mostly observed in the above-mentioned PLL-based estimation schemes. The consequence of this PI-based LF structure includes that these speed estimation schemes cannot achieve zero steady-state errors, where the input has a frequency ramp. Thus, the conventional PLL-based speed estimation schemes may present estimation errors in certain operation conditions, which may happen in practice, e.g., during acceleration and deceleration process. To address this issue, several solutions have been reported in the literature. Among them, the most straightforward methods employ the type-3 PLL-based scheme [25], [26]. In the type-3 PLL scheme, the PI-based LF is replaced with a new-type LF that has two poles at the origin. With this, this scheme ensures zero steady-state errors under frequency ramps. Although the type-3 PLL scheme has the characteristic of tracking frequency ramp accurately, the negative gain margin is also observed in this scheme. In addition, an attempt named as the ZPLL scheme was made in [27] to improve the estimation performance during frequency ramps. The ZPLL scheme was implemented by introducing a phase angle error compensation unit on the basis of the conventional PLL scheme. The compensation unit, serving as an open-loop compensator, makes the ZPLL scheme provide the same characteristic of the type-3 PLL system, while maintaining the acceptable dynamics. However, the ZPLL scheme may not work effectively under abnormal frequencies (i.e., the frequencies deviate from the nominal grid frequency). Additionally, the dual-loop PLL scheme becomes a popular alternative, which has been explored in [28]-[30]. Notably, most of the dual-loop PLL schemes enhance the estimation performance during frequency ramps at the expense of increasing system order, and hence, slowing transient response.

In light of the above, this paper attempts to achieve speed estimation by using the steady-state linear Kalman filter-based phase-locked loop (hereafter, referred to as the SSLKF-PLL scheme) for speed-sensorless control of LIM drives, which is the extended version of [31] and more details are included in this paper. The remaining of this paper begins with the mathematical model of the SSLKF-PLL system, as presented in Section II, which is followed by the implementation of the SSLKF-PLL scheme. Notably, the pre-filters and an amplitude normalization (AN) unit are employed to improve the disturbance rejection capability of the proposed scheme, as detailed in Section III, where the dynamic performance of the SSLKF-PLL scheme in response to different inputs is also analyzed. In Section IV, the parameter tuning using the derived small signal model of the proposed SSLKF-PLL scheme is elaborated. Experimental tests are performed to investigate the effectiveness of the SSLKF-PLL scheme, and the corresponding results are presented in Section V. Finally, Section VI provides the concluding remarks.

## II. Model of the SSLKF-PLL System

The SSLKF-PLL system receives considerable attention for synchronization in power and energy applications, e.g., microgrids and grid-connected converters, because of its acceptable performance and robustness [32]-[35]. In the SSLKF-PLL system, a correction unit is used to replace the PI-based LF in the synchronous reference frame PLL (SRF-PLL) system. In addition, a prediction unit is employed as the voltage-controlled oscillator (VCO) of the SRF-PLL system.

According to the number of state variables in the prediction unit, the SSLKF-PLL system, generally, can be categorized as two-state and three-state SSLKF-PLL systems. In this paper, the proposed speed estimation scheme is based on the three-state SSLKF-PLL system, aiming at tracking frequency ramp accurately (it will be demonstrated soon). The prediction unit of the three-state SSLKF-PLL system can be described as

$$\begin{cases} \boldsymbol{x}(\lambda) = \boldsymbol{A}\boldsymbol{x}(\lambda-1) \\ \boldsymbol{y}(\lambda) = \boldsymbol{C}\boldsymbol{x}(\lambda) \end{cases} \tag{1}$$

where $\boldsymbol{x}$, $\boldsymbol{y}$, $\boldsymbol{A}$, $\boldsymbol{C}$ and $\lambda$ are the input variable matrix, the output variable matrix, the state matrix, the output matrix and the sampling instant, respectively. Additionally,

$$\boldsymbol{x}^T = [\theta \quad \omega \quad a] \quad \boldsymbol{A} = \begin{bmatrix} 1 & T_s & T_s^2/2 \\ 0 & 1 & T_s \\ 0 & 0 & 1 \end{bmatrix} \quad \boldsymbol{C} = \begin{bmatrix} 1 & 0 & 0 \end{bmatrix}$$

in which $\theta$, $\omega$, $a$ and $T_s$ are the phase angle, the angular frequency, the angular acceleration and the sampling time, respectively. Furthermore, $a = d\omega/dt$. Based on (1), the state prediction and state correction units can be described as

$$\begin{cases} \tilde{\boldsymbol{x}}(\lambda) = \boldsymbol{A}\hat{\boldsymbol{x}}(\lambda-1) \\ \hat{\boldsymbol{x}}(\lambda) = \tilde{\boldsymbol{x}}(\lambda) + \boldsymbol{k}\theta_e(\lambda) \end{cases} \tag{2}$$

where $\tilde{\boldsymbol{x}}$, $\hat{\boldsymbol{x}}$, $\boldsymbol{k}$ and $\theta_e$ are the prediction state variable, the correction state variable, the adjustment matrix and the phase error, respectively, with

$$\boldsymbol{k}^T = [k_1 \quad k_2 \quad k_3] \qquad \theta_e = \theta(\lambda) - \tilde{\theta}(\lambda) \tag{3}$$

Here, $k_1$, $k_2$ and $k_3$ are the gains of the adjustment matrix. $\tilde{\theta}$ is the estimated phase by the SSLKF-PLL system.

According to (1) and (2), the detailed structure of the SSLKF-PLL system is shown in Fig. 1(a). After several mathematical operations, the structure of the SSLKF-PLL system can also be described in the *s*-domain, as shown in Fig. 1(b) (the detailed derivation of the model is given in Appendix). Due to the very small gain (i.e., half of sampling time) of the highlighted path (orange color line) in Fig. 1(b), this path is generally neglected as it has a negligible influence on the estimation performance.

This article has been accepted for publication in a future issue of this journal, but has not been fully edited. Content may change prior to final publication. Citation information: DOI 10.1109/TIA.2020.3008673, IEEE Transactions on Industry Applications



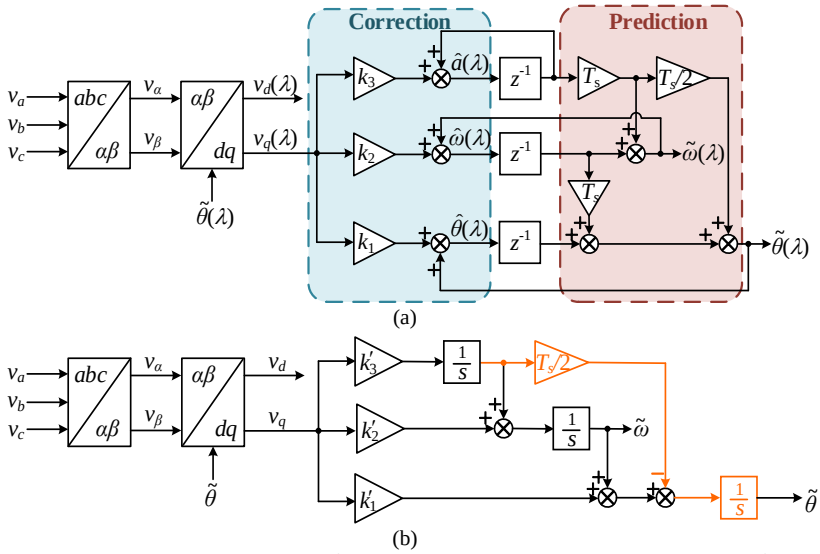


Fig. 1. Block diagrams of the SSLKF-PLL system: (a) the *z*-domain of the SSLKF-PLL system and (b) the *s*-domain of the SSLKF-PLL system, where $k_1' = k_1/T_s$, $k_2' = k_2/T_s$, and $k_3' = k_3/T_s$, with $T_s$ being the sampling time.

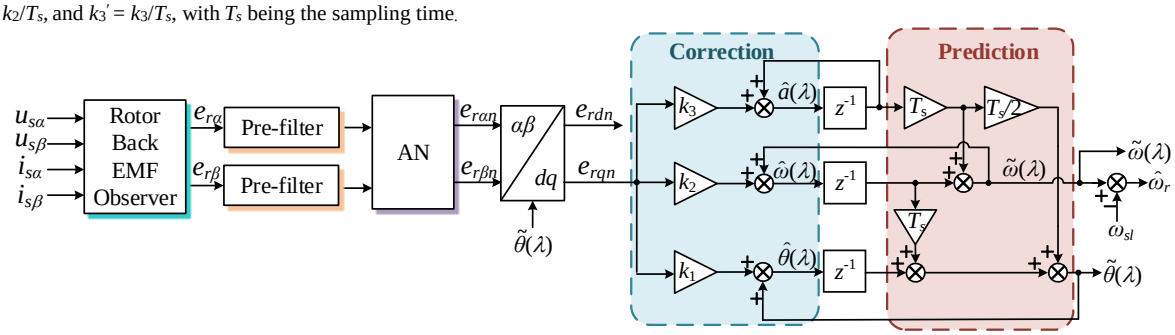


Fig. 2. Block diagram of the proposed speed estimation scheme based on the SSLKF-PLL system, which includes the rotor back EMF observer, the pre-filters, the amplitude normalization (AN) unit and the ideal SSLKF-PLL.

## III. Speed Estimation Scheme Based on the SSLKF-PLL

In this section, the implementation of the SSLKF-PLL scheme is detailed. Meanwhile, the disturbance rejection of the SSLKF-PLL scheme will be discussed. The dynamic performance is also analyzed.

### A. SSLKF-PLL Scheme

One of the issues in the power and energy applications is the power quality, where harmonics, imbalance, voltage sags and swells may appear in the system. These disturbances can be regarded as a major challenge to the PLL. This situation still occurs in the speed-sensorless control of LIM drives. As an example, the non-idealities in the rotor back electromotive force signals (EMFs) (which have large harmonics or subject to parameter variations) may adversely affect the performance of the SSLKF-PLL scheme for speed estimation. With this concern, in practice, the SSLKF-PLL scheme is implemented with disturbance rejection, as depicted in Fig. 2.

Observations in Fig. 2 indicate that the SSLKF-PLL scheme consists of four parts, i.e., the rotor back EMF observer, the pre-filters, the AN unit, and the ideal SSLKF-PLL. The rotor back EMF observer provides the estimated rotor back EMFs, as the inputs of the SSLKF-PLL scheme. More specifically, the pre-filters offer the harmonic rejection, and the AN unit is employed to mitigate the effect of parameter variations. The estimated speed information (including the estimated rotor speed and rotor flux phase) is eventually obtained through the ideal SSLKF-PLL. According to Fig. 2, when the angular speed is estimated, the estimated rotor speed can be given as

$$\hat{\omega}_r = \tilde{\omega} - \omega_{sl} \tag{4}$$

where $\omega_{sl}$ is the slip speed. Subsequently, the estimated linear speed can be expressed as

$$\hat{v} = (2\hat{\omega}_r \xi)/(p\pi) \tag{5}$$

in which $p$ and $\xi$ are the pole number and the pole distance, respectively. Notice that the estimated rotor flux phase $\tilde{\theta}$, as the rotor flux orientation phase, is also provided by using the SSLKF-PLL scheme.

### B. Rotor Back EMF Observer

The block diagram of the rotor back EMF observer is presented in Fig. 3, where $\boldsymbol{u_s}$, $\boldsymbol{i_s}$, $\boldsymbol{\Psi_{dq}}$, $\boldsymbol{\Psi_r^r}$, $\hat{\boldsymbol{\Psi}}_s$, $\hat{\boldsymbol{\Psi}}_r$, $\hat{\boldsymbol{e}}_r$, $\hat{\theta}_r$ and $R_s$ are the stator voltage vector, the stator current vector, the rotor flux vector in the synchronous reference frame (*dq*-frame), the rotor flux vector in the stationary reference frame (*αβ*-frame), the estimated stator flux vector, the estimated rotor flux vector, the estimated rotor back EMF vector,

This article has been accepted for publication in a future issue of this journal, but has not been fully edited. Content may change prior to final publication. Citation information: DOI 10.1109/TIA.2020.3008673, IEEE Transactions on Industry Applications



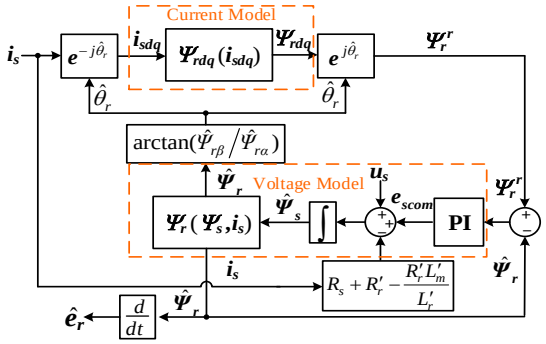


Fig. 3. Block diagram of the rotor back EMF observer.

the estimated rotor flux phase and the stator resistance of the LIM, correspondingly. Moreover, $\boldsymbol{u_s} = [u_{s\alpha}\ u_{s\beta}]^T$, $\boldsymbol{i_s} = [i_{s\alpha}\ i_{s\beta}]^T$, $\boldsymbol{i_{sdq}} = [i_{sd}\ i_{sq}]^T$, $\boldsymbol{\Psi_{rdq}} = [\Psi_{rd}\ \Psi_{rq}]^T$, $\boldsymbol{\Psi_r^r} = [\Psi_{r\alpha}{}^r\ \Psi_{r\beta}{}^r]^T$, $\hat{\boldsymbol{\Psi}}_s = [\hat{\Psi}_{sa}\ \hat{\Psi}_{s\beta}]^T$, $\hat{\boldsymbol{\Psi}}_r = [\hat{\Psi}_{ra}\ \hat{\Psi}_{r\beta}]^T$, $\hat{\boldsymbol{e}}_r = [\hat{e}_{ra}\ \hat{e}_{r\beta}]^T$.

The current model (CM) in the synchronous reference frame can be obtained as

$$\begin{cases} \Psi_{rd} = |\Psi_r| = \dfrac{L_m' - R_r' T_r'}{1 + pT_r'} i_{sd} \\ \Psi_{rq} = 0 \end{cases} \tag{6}$$

where $T_r'$, $L_m'$, $R_r'$, $p$ and $i_{sd}$ are the rotor time constant, the magnetizing inductance, the rotor resistance of the LIM, the differential operator and the $d$-axis component of the stator current, respectively. And,

$$i_{sd} = \cos(\hat{\theta}_r) i_{s\alpha} + \sin(\hat{\theta}_r) i_{s\beta} \tag{7}$$

Then, the rotor flux in the rotor coordinate system can be written as

$$\begin{bmatrix} \Psi_{r\alpha}^r \\ \Psi_{r\beta}^r \end{bmatrix} = \begin{bmatrix} \cos(\hat{\theta}_r) & -\sin(\hat{\theta}_r) \\ \sin(\hat{\theta}_r) & \cos(\hat{\theta}_r) \end{bmatrix} \begin{bmatrix} \Psi_{rd} \\ \Psi_{rq} \end{bmatrix} \tag{8}$$

Subsequently, the voltage model (VM) in the stationary reference frame can be given by

$$\begin{bmatrix} \hat{\Psi}_{r\alpha} \\ \hat{\Psi}_{r\beta} \end{bmatrix} = \frac{L_r'}{L_m'} \begin{bmatrix} \hat{\Psi}_{s\alpha} \\ \hat{\Psi}_{s\beta} \end{bmatrix} - \frac{L_s' L_r' - L_m'^2}{L_r'} \begin{bmatrix} i_{s\alpha} \\ i_{s\beta} \end{bmatrix} - \frac{R_r'}{L_m'} \left( \int \begin{bmatrix} \hat{\Psi}_{r\alpha} \\ \hat{\Psi}_{r\beta} \end{bmatrix} dt \right) \tag{9}$$

with $L_s'$ being the stator inductance of the LIM. The estimated stator flux in the stationary reference frame is written as

$$\begin{bmatrix} \hat{\Psi}_{s\alpha} \\ \hat{\Psi}_{s\beta} \end{bmatrix} = \begin{bmatrix} \int [u_{s\alpha} - \left( R_s + R_r' - \dfrac{R_r' L_m'}{L_r'} \right) i_{s\alpha} + e_{com\alpha}] \\ \int [u_{s\beta} - \left( R_s + R_r' - \dfrac{R_r' L_m'}{L_r'} \right) i_{s\beta} + e_{com\beta}] \end{bmatrix} \tag{10}$$

where $e_{com\alpha}$ and $e_{com\beta}$ are the $\alpha$- and $\beta$-axis compensated components of the stator back EMFs, respectively. The compensated signals of the stator back EMFs are used to eliminate the effect of the DC offsets. And, they can be obtained by using a PI controller as

$$\begin{bmatrix} e_{com\alpha} \\ e_{com\beta} \end{bmatrix} = \underbrace{\left( k_p + \frac{k_i}{s} \right)}_{PI} \begin{bmatrix} \Psi_{r\alpha}^r - \hat{\Psi}_{r\alpha} \\ \Psi_{r\beta}^r - \hat{\Psi}_{r\beta} \end{bmatrix} \tag{11}$$

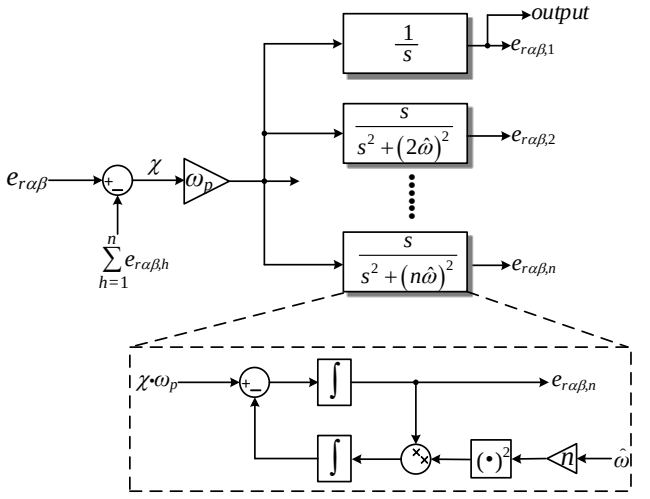


Fig. 4. Block diagram of the pre-filter, where mutiple adaptive filters are adopted to matigate the effect of harmonics in the rotor back EMFs.

in which $k_p$ and $k_i$ are the gains of the PI controller in the rotor back EMF observer. Accordingly, the estimated rotor back EMFs can be expressed as

$$\begin{bmatrix} \hat{e}_{r\alpha} \\ \hat{e}_{r\beta} \end{bmatrix} = \frac{d}{dt} \begin{bmatrix} \hat{\Psi}_{r\alpha} \\ \hat{\Psi}_{r\beta} \end{bmatrix} = \frac{1}{T_s} \begin{bmatrix} \hat{\Psi}_{r\alpha}(\lambda) - \hat{\Psi}_{r\alpha}(\lambda - 1) \\ \hat{\Psi}_{r\beta}(\lambda) - \hat{\Psi}_{r\beta}(\lambda - 1) \end{bmatrix} \tag{12}$$

Moreover, the estimated rotor flux phase can be calculated as

$$\hat{\theta}_r = \arctan\left( \frac{\hat{\Psi}_{r\beta}}{\hat{\Psi}_{r\alpha}} \right) \tag{13}$$

From the above-mentioned analysis, the rotor back EMF observer combines the advantages of the CM with the advantages of the VM. With this, the rotor back EMFs can work well in a wide speed range and have the capability to deal with the DC offsets.

### C. *Pre-filter Stage*

As discussed previously, the pre-filters enable the SSLKF-PLL scheme to alleviate the effect of harmonics in the rotor back EMFs. In practice, there are abundant harmonics appearing in the rotor back EMFs, which are mainly attributable to the inverter nonlinearity. Moreover, these harmonics may lead to the ripples in the estimated parameters. For example, an $h$-order harmonic component can result in an ($h$-1)-order harmonic ripple, which obviously degrades the speed estimation. Using the pre-filters is expected to improve the speed estimation quality in the presence of harmonics. The structure of the pre-filter in the SSLKF-PLL scheme is illustrated in Fig. 4. It is indicated in Fig. 4 that the pre-filter consists of a set of adaptive filters, and each unit will extract an individual frequency component. Notably, due to the parallel structure, the pre-filter can simultaneously extract various harmonics from the rotor back EMFs. Subsequently, the selective harmonic components are subtracted from the rotor back EMFs. This enables mitigating the harmonics of interest to improve the estimation performance.

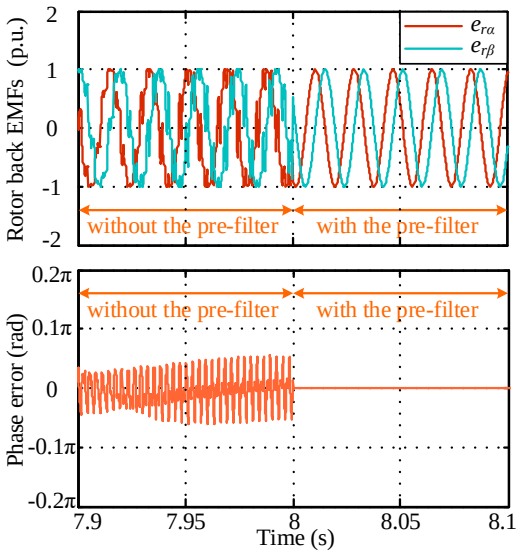


Fig. 5. Performance comparison of the SSLKF-PLL scheme with and without the pre-filters.

The effectiveness of the pre-filters is investigated in Fig. 5, where the rotor back EMFs and phase estimation error are presented. The results show that the rotor back EMFs may experience serious distortions without the assistance of the pre-filters. Consequently, oscillations appear in the estimated quantities. In contrast, when the pre-filters are enabled, the rotor back EMFs will be purely sinusoidal, leading to accurate estimation by the SSLKF-PLL scheme, as shown in Fig. 5. In all, it has been demonstrated that the pre-filters in the SSLKF-PLL scheme can offer a satisfactory performance in term of harmonics rejection.

### *D. Amplitude Normalization Unit*

The major problem for the model-based speed estimation schemes is the parameter variations. Particularly, the problem of stator resistance variations is noticeable, as it may compromise the speed estimation performance and even aggravate the stability problem. To tackle this issue, incorporating the stator resistance on-line identification scheme is a popular solution due to its high robustness [36]-[39]. This scheme, however, suffers from heavy computational burden and it is complicated. Considering this, an AN unit is adopted in the SSLKF-PLL scheme, and the structure of the AN unit is shown in Fig. 6. The performance of the AN unit is analyzed as follows. According to the AN scheme presented in Fig. 6, it can be obtained that

$$\begin{cases} e_{r\alpha n} = \dfrac{e_{r\alpha}}{\sqrt{(e_{r\alpha})^2 + (e_{r\beta})^2}} \\ e_{r\beta n} = \dfrac{e_{r\beta}}{\sqrt{(e_{r\alpha})^2 + (e_{r\beta})^2}} \end{cases} \tag{14}$$

where $e_{r\alpha n}$ and $e_{r\beta n}$ are the rotor back EMFs passing through the AN scheme. The rotor back EMFs considering the parameter variations can be described as

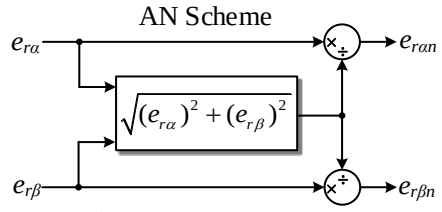


Fig. 6. Block diagram of the AN scheme.

$$\begin{cases} e_{r\alpha d} = e_{r\alpha} + \Delta e_{r\alpha} \\ e_{r\beta d} = e_{r\beta} + \Delta e_{r\beta} \end{cases} \tag{15}$$

in which $e_{r\alpha d}$, $e_{r\beta d}$, $\Delta e_{r\alpha}$ and $\Delta e_{r\beta}$ are the rotor back EMFs considering the parameter variations and the variations of the rotor back EMFs after parameter variations. The rotor back EMFs considering parameter variations, when passing through the AN unit, are written as

$$\begin{cases} e_{r\alpha dn} = \dfrac{(e_{r\alpha} + \Delta e_{r\alpha})}{\sqrt{(e_{r\alpha} + \Delta e_{r\alpha})^2 + (e_{r\beta} + \Delta e_{r\beta})^2}} \\ e_{r\beta dn} = \dfrac{(e_{r\beta} + \Delta e_{r\beta})}{\sqrt{(e_{r\alpha} + \Delta e_{r\alpha})^2 + (e_{r\beta} + \Delta e_{r\beta})^2}} \end{cases} \tag{16}$$

where $e_{r\alpha dn}$ and $e_{r\beta dn}$ are the rotor back EMFs considering the parameter variations when passing through the AN scheme. Considering the pre-filters can effectively mitigate the effect of harmonics, the rotor back EMFs can be expressed as

$$\begin{cases} e_{r\alpha} = V\cos\theta \\ e_{r\beta} = V\sin\theta \end{cases} \tag{17}$$

with $V$ and $\theta$ being the amplitude and phase of the rotor back EMFs. Accordingly, the rotor back EMFs considering the parameter variations can be obtained as

$$\begin{cases} e_{r\alpha d} = (V + \Delta V)\cos\theta \\ e_{r\beta d} = (V + \Delta V)\sin\theta \end{cases} \tag{18}$$

where $\Delta V$ denotes the amplitude variation of the rotor back EMFs when considering the parameter variations. Substituting (18) into (16) yields

$$\begin{cases} e_{r\alpha dn} = \dfrac{(V + \Delta V)\cos\theta}{(V + \Delta V)} = \cos\theta \\ e_{r\beta dn} = \dfrac{(V + \Delta V)\sin\theta}{(V + \Delta V)} = \sin\theta \end{cases} \tag{19}$$

Similarly, substituting (17) into (14) gives

$$\begin{cases} e_{r\alpha n} = \dfrac{V\cos\theta}{V} = \cos\theta \\ e_{r\beta n} = \dfrac{V\sin\theta}{V} = \sin\theta \end{cases} \tag{20}$$

Based on (19) and (20), it is indicated that the rotor back EMFs work well after the parameter variations, with the assistance of the AN unit. The performance of the AN unit is also explored. The corresponding test results, which are shown in Fig. 7, indicate that the performance of the rotor back EMFs is acceptable after the stator resistance variations, and accordingly, the estimation performance is guaranteed.

This article has been accepted for publication in a future issue of this journal, but has not been fully edited. Content may change prior to final publication. Citation information: DOI 10.1109/TIA.2020.3008673, IEEE Transactions on Industry Applications



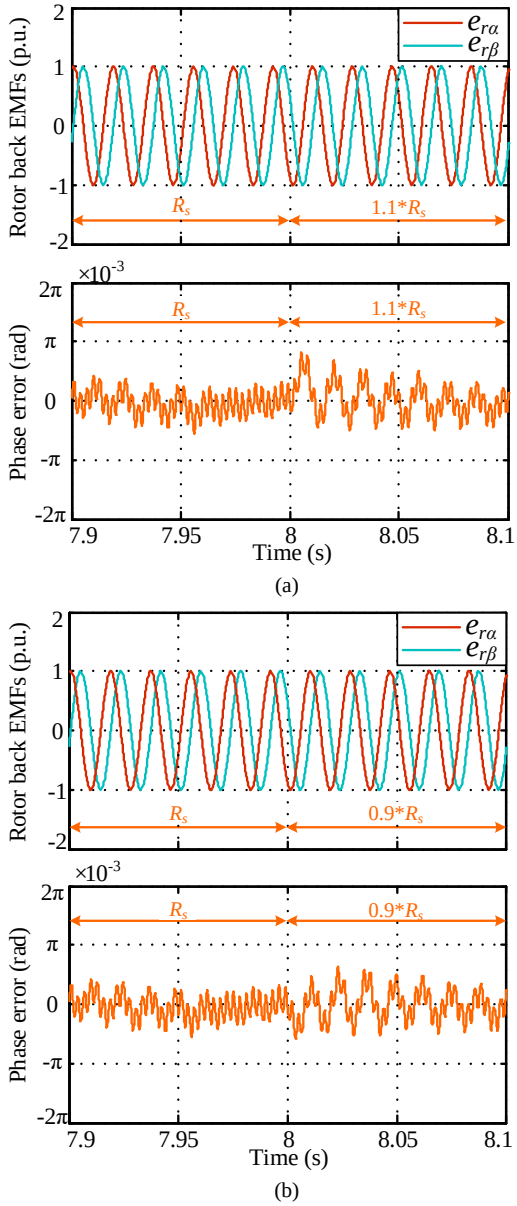


Fig. 7. Performance of the SSLKF-PLL scheme with the case of parameter variations: (a) the performance with the stator resistance increases and (b) the performance with the stator resistance decreases.

### *E. Dynamic Performance Analysis*

To analyze the dynamic performance of the SSLKF-PLL scheme, the small signal model should be obtained. Assuming that the pre-filters and the AN unit can successfully reject the disturbances, the small signal model of the SSLKF-PLL scheme is depicted in Fig. 8, where $\omega$, $\theta$, $\tilde{\omega}$, $\tilde{\theta}$ and $\theta_e$ are the input frequency, the input phase, the estimated frequency, the estimated phase and the phase estimation error, respectively. According to Fig. 8, it can be obtained as

$$[\theta(s)-\tilde{\theta}(s)][k_1'+(k_2'+\frac{k_3'}{s})\frac{1}{s}]\frac{1}{s}=\tilde{\theta}(s) \tag{21}$$

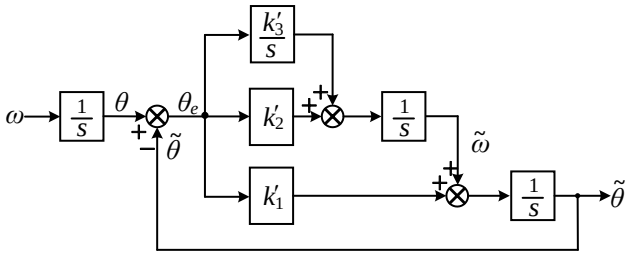


Fig. 8. Small signal model of the SSLKF-PLL scheme.

$$[\omega(s)\frac{1}{s}-\tilde{\theta}(s)][(k_2'+\frac{k_3'}{s})\frac{1}{s}]=\tilde{\omega}(s) \tag{22}$$

Subsequently, the open-loop transfer functions of the SSLKF-PLL scheme can be given as

$$G_{ol}^{\omega}(s)=\frac{\tilde{\omega}(s)}{\omega(s)-\tilde{\omega}(s)}=\frac{k_2's+k_3'}{s^2(s+k_1')} \tag{23}$$

$$G_{ol}^{\theta}(s)=\frac{\tilde{\theta}(s)}{\theta(s)-\tilde{\theta}(s)}=\frac{k_1's^2+k_2's+k_3'}{s^3} \tag{24}$$

where the $G_{ol}{}^{\omega}(s)$ and $G_{ol}{}^{\theta}(s)$ are the frequency and phase open-loop transfer functions of the SSLKF-PLL scheme, respectively. Accordingly, the frequency- and phase-error transfer functions can be written as

$$G_e^{\omega}(s)=\frac{\omega(s)-\tilde{\omega}(s)}{\omega(s)}=\frac{1}{1+G_{ol}^{\omega}(s)}=\frac{s^2(s+k_1')}{s^3+k_1's^2+k_2's+k_3'} \tag{25}$$

$$G_e^{\theta}(s)=\frac{\theta(s)-\tilde{\theta}(s)}{\theta(s)}=\frac{1}{1+G_{ol}^{\theta}(s)}=\frac{s^3}{s^3+k_1's^2+k_2's+k_3'} \tag{26}$$

in which $G_e{}^{\omega}(s)$ and $G_e{}^{\theta}(s)$ are the frequency- and phase-error transfer functions of the SSLKF-PLL scheme, respectively. Three input signals are applied in the SSLKF-PLL scheme, i.e., a phase jump, a frequency jump and a frequency ramp, which are described as

$$\omega_{i1}(s)=m,\quad \theta_{i1}(s)=\frac{m}{s} \tag{27}$$

$$\omega_{i2}(s)=\frac{q}{s},\quad \theta_{i2}(s)=\frac{q}{s^2} \tag{28}$$

$$\omega_{i3}(s)=\frac{h}{s^2},\quad \theta_{i3}(s)=\frac{h}{s^3} \tag{29}$$

with $m$, $q$ and $h$ being the gains of the input signals. Substituting (27)-(29) into (25), the frequency-error transfer functions are obtained with these inputs as

$$\Delta\omega_1(s)=\omega_{i1}(s)G_e^{\omega}(s)=\frac{ms^2(s+k_1')}{s^3+k_1's^2+k_2's+k_3'} \tag{30}$$

$$\Delta\omega_2(s)=\omega_{i2}(s)G_e^{\omega}(s)=\frac{qs(s+k_1')}{s^3+k_1's^2+k_2's+k_3'} \tag{31}$$

$$\Delta\omega_3(s)=\omega_{i3}(s)G_e^{\omega}(s)=\frac{h(s+k_1')}{s^3+k_1's^2+k_2's+k_3'} \tag{32}$$

Similarly, the corresponding phase-error transfer functions with these inputs are described as

$$\Delta\theta_1(s)=\theta_{i1}(s)G_e^{\theta}(s)=\frac{ms^2}{s^3+k_1's^2+k_2's+k_3'} \tag{33}$$

$$\Delta\theta_2(s)=\theta_{i2}(s)G_e^{\theta}(s)=\frac{qs}{s^3+k_1's^2+k_2's+k_3'} \tag{34}$$

$$\Delta\theta_3(s)=\theta_{i3}(s)G_e^{\theta}(s)=\frac{h}{s^3+k_1's^2+k_2's+k_3'} \tag{35}$$

Applying the final value theorem to (30)-(35) yields

$$\Delta\omega_{ess1}=\lim_{s\to0}s\Delta\omega_1(s)=\lim_{s\to0}s\frac{ms^2(s+k_1')}{s^3+k_1's^2+k_2's+k_3'}=0 \tag{36}$$

$$\Delta\omega_{ess2}=\lim_{s\to0}s\Delta\omega_2(s)=\lim_{s\to0}s\frac{qs(s+k_1')}{s^3+k_1's^2+k_2's+k_3'}=0 \tag{37}$$

$$\Delta\omega_{ess3}=\lim_{s\to0}s\Delta\omega_3(s)=\lim_{s\to0}s\frac{h(s+k_1')}{s^3+k_1's^2+k_2's+k_3'}=0 \tag{38}$$

$$\Delta\theta_{ess1}=\lim_{s\to0}s\Delta\theta_1(s)=\lim_{s\to0}s\frac{ms^2}{s^3+k_1's^2+k_2's+k_3'}=0 \tag{39}$$

$$\Delta\theta_{ess2}=\lim_{s\to0}s\Delta\theta_2(s)=\lim_{s\to0}s\frac{qs}{s^3+k_1's^2+k_2's+k_3'}=0 \tag{40}$$

$$\Delta\theta_{ess3}=\lim_{s\to0}s\Delta\theta_3(s)=\lim_{s\to0}s\frac{h}{s^3+k_1's^2+k_2's+k_3'}=0 \tag{41}$$

From (36)-(41), it can be seen that the SSLKF-PLL scheme can track the phase jump and frequency jump with zero steady-state errors. Remarkably, it also indicates that the SSLKF-PLL scheme has the capability in tracking the frequency ramp accurately.

To demonstrate the aforementioned analysis, case studies are performed, including an amplitude jump of +10 A, a phase jump of +20 °, a frequency jump of +5 Hz and a frequency ramp of +10 Hz/s. The corresponding results are presented in Fig. 9. According to Fig. 9, it is known that the SSLKF-PLL scheme behaves well with the amplitude jump, the phase jump and the frequency jump. More importantly, notice that the SSLKF-PLL scheme can achieve accurate estimation when the inputs have a frequency ramp. This is in consistency with the above analysis.

## IV. Parameter Tuning of the SSLKF-PLL Scheme

To ensure the performance of the proposed estimation scheme, it is necessary to explore the parameter tuning of the SSLKF-PLL scheme. For convenience, the frequency open-loop transfer function (23) is rewritten as

$$G_{ol}^{\omega}(s)=k\frac{(s+\omega_z)}{s^2(s+\omega_p)} \tag{42}$$

in which $k$, $\omega_p$ and $\omega_z$ are the gains of the SSLKF-PLL scheme, respectively, and moreover,

$$k_1'=\omega_p \quad k_2'=k \quad k_3'=k\omega_z$$

Based on (42), the amplitude-frequency and phase-frequency characteristics are described as

$$\left|A(j\omega)\right|=\left|G_{ol}^{\omega}(j\omega)\right|=k\frac{\sqrt{\left(\omega^2+\omega_z{}^2\right)}}{\omega^2\sqrt{\left(\omega^2+\omega_p{}^2\right)}} \tag{43}$$

$$\varphi=\angle G_{ol}^{\omega}(j\omega)=\arctan\frac{\omega}{\omega_z}-\arctan\frac{\omega}{\omega_p}-\pi \tag{44}$$

Accordingly, the amplitude-frequency and phase-frequency characteristics of the SSLKF-PLL scheme at the crossover frequency $\omega_c$ are given as

$$\left|A(j\omega_c)\right|=\left|G_{ol}(j\omega_c)\right|=k\frac{\sqrt{\left(\omega_c{}^2+\omega_z{}^2\right)}}{\omega_c{}^2\sqrt{\left(\omega_c{}^2+\omega_p{}^2\right)}}=1 \tag{45}$$

$$\angle G_{ol}(j\omega_c)=\arctan\frac{\omega_c}{\omega_z}-\arctan\frac{\omega_c}{\omega_p}-\pi \tag{46}$$

Subsequently, the phase margin (PM) is calculated as

$$PM=\angle G_{ol}(j\omega_c)-(-\pi)=\underbrace{\arctan\left(\frac{\omega_c}{\omega_z}\right)}_{\varphi_z}-\underbrace{\arctan\left(\frac{\omega_c}{\omega_p}\right)}_{\varphi_p} \tag{47}$$

with,

$$\begin{aligned}\tan\varphi_p&=\frac{\omega_c}{\omega_p}\Rightarrow\cos\varphi_p=\frac{\omega_p}{\sqrt{\omega_p{}^2+\omega_c{}^2}}\\ \tan\varphi_z&=\frac{\omega_c}{\omega_z}\Rightarrow\sin\varphi_z=\frac{\omega_c}{\sqrt{\omega_z{}^2+\omega_c{}^2}}\end{aligned} \tag{48}$$

Substituting (48) into (45), the crossover frequency $\omega_c$ can be expressed as

$$\omega_c=\frac{k}{\omega_p}\frac{\omega_p\sqrt{\left(\omega_c{}^2+\omega_z{}^2\right)}}{\omega_c\sqrt{\left(\omega_c{}^2+\omega_p{}^2\right)}}=\frac{k}{\omega_p}\frac{\cos\varphi_p}{\sin\varphi_z} \tag{49}$$

Taking the derivative of (47) with the crossover frequency $\omega_c$ as the variable, it is given by

$$\frac{\partial(PM)}{\partial(\omega_c)}=\frac{\omega_z}{\omega_z{}^2+\omega_c{}^2}-\frac{\omega_p}{\omega_p{}^2+\omega_c{}^2} \tag{50}$$

Considering $\partial PM/\partial\omega_c=0$, it yields

$$\omega_c=\sqrt{\omega_p\omega_z} \tag{51}$$

Substituting (51) into (49), it can be obtained as

$$\omega_c=\frac{k}{\omega_p} \tag{52}$$

Supposing that $\omega_p=g^2\omega_z$, it gives

$$\begin{cases}\omega_p=g\omega_c\\ \omega_z=\omega_c/g\\ k=g\omega_c{}^2\end{cases} \tag{53}$$

with $g$ being a positive constant. Accordingly, the PM can be rewritten as

This article has been accepted for publication in a future issue of this journal, but has not been fully edited. Content may change prior to final publication. Citation information: DOI 10.1109/TIA.2020.3008673, IEEE Transactions on Industry Applications



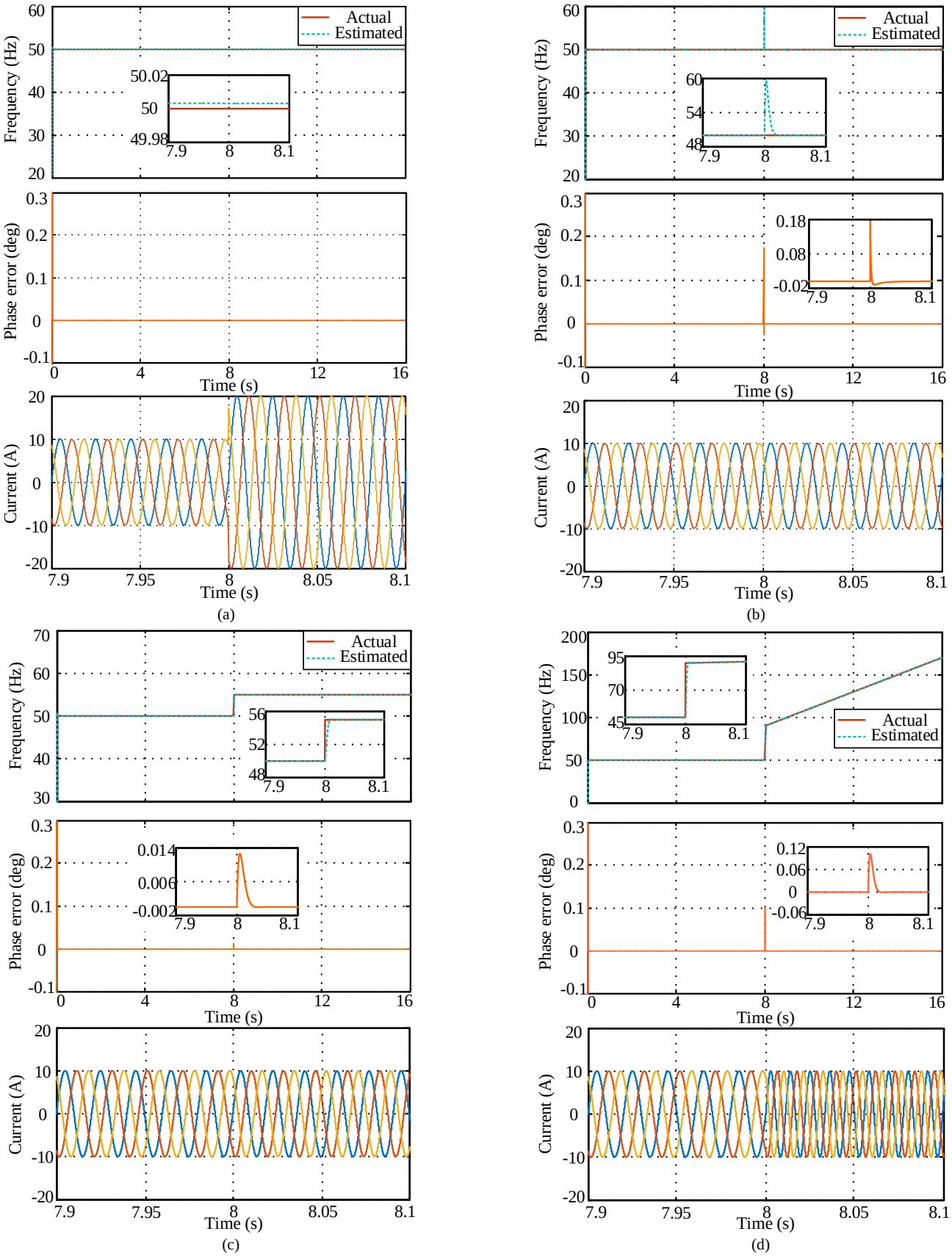


Fig. 9. Dynamic performance of the SSLKF-PLL scheme with different inputs: (a) the performance with amplitude jump of +10 A, (b) the performance with phase jump of +20 °, (c) the performance with frequency jump of +5 Hz, and (d) the performance with frequency ramp of +10 Hz/s.

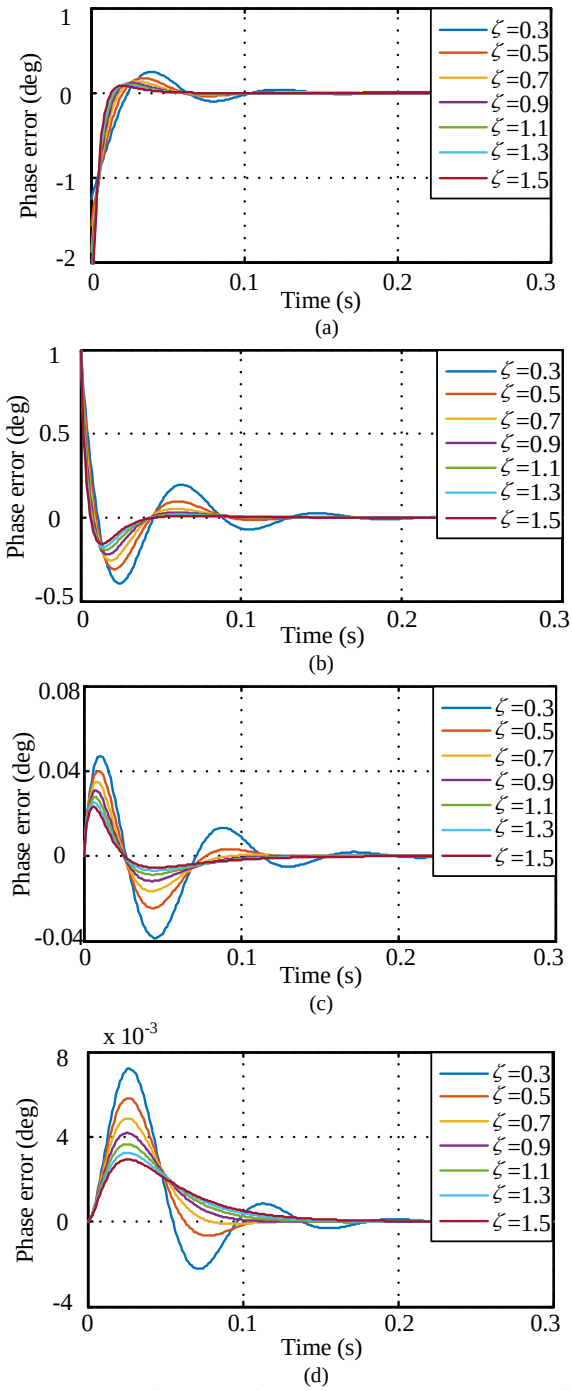


Fig. 10. Dynamic performance of the SSLKF-PLL scheme with different values of $\zeta$ under different inputs: (a) the performance under the amplitude jump, (b) the performance under the phase jump, (c) the performance under the frequency jump, and (d) the performance under the frequency ramp.

$$PM = \arctan\left(\frac{g^2-1}{2g}\right) \tag{54}$$

in which $g$ can be rewritten as

$$g = 2\zeta + 1 \tag{55}$$

where $\zeta$ is defined as the damping factor. Substituting (53) and (55) into (25), the frequency-error transfer function can be rewritten as

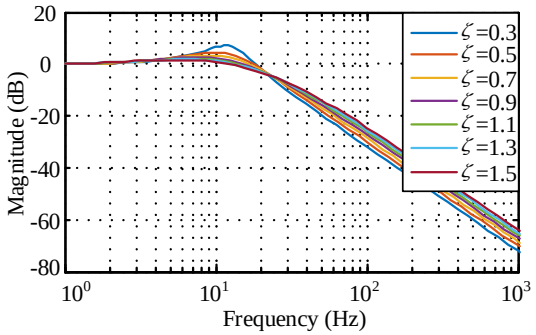


Fig. 11. Closed-loop Bode plots of the of the SSLKF-PLL scheme with different values of $\zeta$.

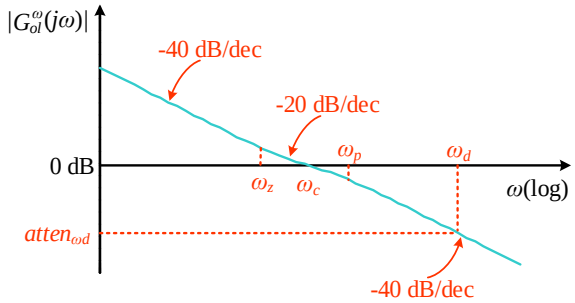


Fig. 12. Logarithmic magnitude plot of the open-loop transfer function of the SSLKF-PLL scheme.

$$G_e^{\omega}(s) = \frac{1}{1+G_{ol}^{\omega}(s)} = \frac{s^2\left[s+(2\zeta+1)\omega_c\right]}{(s+\omega_c)(s^2+2\zeta\omega_c s+\omega_c{}^2)} \tag{56}$$

Based on the above information, it is interesting to find that the number of degrees of freedom is reduced to two, which means the control system parameters (e.g., $k_1'$, $k_2'$ and $k_3'$) can be tuned by determining $\omega_c$ and $\zeta$.

The value of $\zeta$ is tuned first. Fig. 10 presents the dynamic performance of the SSLKF-PLL scheme with different values of $\zeta$. Observations in Fig. 10 suggest that a smaller value of $\zeta$ leads to a large resonant peak, while a larger value of $\zeta$ results in slow dynamics with a reduced overshoot. To further analyze this impact, the closed-loop Bode plots of the SSLKF-PLL scheme with different values of $\zeta$ are illustrated in Fig. 11. As expected, the smaller value of $\zeta$ leads to the larger magnitude of the resonant peak, accordingly, more oscillations appearing during the transient response. Therefore, $\zeta$ within the range from 0.6 to 1 should be reasonable to obtain a satisfactory performance in terms of dynamics and steady-state errors [40]-[43]. In this paper, $\zeta$ is set to 0.7 for achieving acceptable dynamic performance of the SSLKF-PLL scheme. When $\zeta$ is determined, the tuning of the crossover frequency $\omega_c$ should be performed. Fig. 12 depicts the amplitude-frequency characteristic curve of the open-loop transfer function of the SSLKF-PLL scheme in (23), and $\omega_d$ is the frequency of the lowest-order harmonic in the rotor back EMFs. According to Fig. 12, it gives

$$atten_{\omega_d} = -20\log\left(\frac{\omega_d{}^2}{\omega_c\omega_p}\right) = -40\log\frac{\omega_d}{\omega_c\sqrt{g}} \tag{57}$$

The crossover frequency $\omega_c$ can then be obtained as

$$\omega_c = \frac{\omega_d}{\sqrt{g}} 10^{\frac{atten_{\omega d}}{40}} \tag{58}$$

According to (58), it is suggested that the crossover frequency $\omega_c$ can be tuned by determining the values of $atten_{\omega d}$ and $\omega_d$. Here, $atten_{\omega d}$ is the amplitude attenuation at the frequency of the lowest-order harmonic $\omega_d$. The value of $atten_{\omega d}$ should also make an appropriate tradeoff between the dynamics and the disturbance rejection capability. This is because a larger value of $atten_{\omega d}$ contributes to the satisfactory dynamics but leads to a poor disturbance rejection capability [40]-[42]. In general, the value of $atten_{\omega d}$ within the range from -15 dB to -20 dB is desirable. In this paper, the value of $atten_{\omega d}$ is set to -16 dB, which is a good choice in terms of the dynamic response and the disturbance rejection capability. Because the pre-filters can effectively filter out the undesired harmonics, the frequency of lowest-order harmonic is set to 10 Hz in this paper. Substituting $\zeta$ = 0.7, $atten_{\omega d}$ = -16 dB and $\omega_d = 20\pi$ rad/s into (58), it gives as

$$\omega_c \approx \frac{\omega_d}{\sqrt{g}} 10^{\frac{atten_{\omega d}}{40}} = \frac{20\pi}{\sqrt{1.5}} * 10^{\frac{-16}{40}} = 6.501\pi \tag{59}$$

Then, the gains of the LF in the SSLKF-PLL scheme can be obtained considering $\omega_c$ and $\zeta$.

## V. Experimental Results

To examine the effectiveness of the SSLKF-PLL scheme, experimental tests are performed. The entire speed-sensorless drive system and the parameters of the LIM drives are presented in Fig. 13 and Table I, respectively.

### A. Algorithm Implementation

As shown in Fig. 13, there are serval units in the speed-sensorless control of the LIM drives: the flux/force command calculation, the decoupling control, the feedforward voltage calculation, the voltage reconstruction, the space vector pulse-width modulation (SVPWM), the Park transformation/ inverse Park transformation and the SSLKF-PLL scheme.

(1) In the flux/force calculation, according to the traction characteristic curve and the rotor flux table which are based on the requirements of the drive system, the rotor flux and the thrust force reference values are calculated.

(2) The decoupling control aims to divide the stator current into two parts, i.e., *d*- and *q*-axis components, and accordingly, these parts are controlled independently. By doing so, the decoupling control is achieved.

(3) The feedforward voltage calculation is introduced into the vector control system to alleviate the adjustment burden of the PI-controller of the stator current, and consequently, improves the dynamic performance of the drive system. In this unit, the estimated angular speed $\tilde{\omega}$ is used to calculate the feedforward voltage.

(4) Regarding the voltage reconstruction, it is used to provide three-phase voltage signals for the speed estimation scheme, which is achieved by using the DC-link voltage and three-phase switching signals. That is,

TABLE I Parameters of the LIM Drives.

| Parameter | Value |
|---|---|
| Rated power | 80 kW |
| Rated voltage | 367 V |
| Rated current | 340 A |
| Stator resistance | 0.15 Ω |
| Rotor resistance | 0.05 Ω |
| Stator inductance | 3.7 mH |
| Rotor inductance | 3.5 mH |
| Magnetizing inductance | 3 mH |
| Pole distance | 216 mm |
| Length of the stator | 2800 mm |
| DC-link voltage | 1500 V |
| Phase of the LIM | 3 |

$$\begin{bmatrix} u_a \\ u_b \\ u_c \end{bmatrix} = \frac{1}{3} U_d^* \begin{bmatrix} 2S_a & -S_b & -S_c \\ -S_a & 2S_b & -S_c \\ -S_a & -S_b & 2S_c \end{bmatrix} \tag{60}$$

where $U_d^*$, $u_{abc}$ and $S_{abc}$ are the DC-link voltage, the reconstructed three-phase voltage signals and three-phase switching signals, respectively.

(5) In the SVPWM unit, notice that the switching frequency is set to 500 Hz, less than 1 kHz, to ensure low switching losses of the LIM drive system.

(6) In the Park transformation/ inverse Park transformation units, the estimated rotor flux phase $\tilde{\theta}$ is used, which is provided by the SSLKF-PLL scheme.

(7) The SSLKF-PLL scheme, instead of the speed sensor, is responsible for providing the estimated linear rotor speed $\hat{v}$, the estimated angular speed $\tilde{\omega}$ and the estimated rotor flux phase $\tilde{\theta}$.

### B. Dynamic Performance Analysis

The dynamic performance of the SSLKF scheme is tested first. The experimental results are shown in Figs. 14-17. Various cases are considered, i.e., an amplitude jump of +10 A, a phase jump of +20 °, a frequency jump of +5 Hz, and a frequency ramp of +10 Hz/s. As evidenced in Figs. 14-17, the SSLKF-PLL scheme behaves satisfactorily during the transients. With the SSLKF-PLL scheme, the performance of speed estimation can be secured.

### C. Speed Estimation Performance

The speed estimation using the SSLKF-PLL scheme with different test cases is also experimentally investigated. Fig. 18 shows the speed estimation performance of the SSLKF-PLL scheme with the load of 1000 N. In addition, the performance of the SSLKF-PLL scheme without the pre-filters is served as a comparison in Fig. 19. As observed, the SSLKF-PLL scheme can achieve accurate speed estimation in this case. In contrast, without the pre-filters, the rotor back EMFs suffer from serious distortions, and consequently, obvious fluctuations appear in the estimated speed, degrading the entire performance.

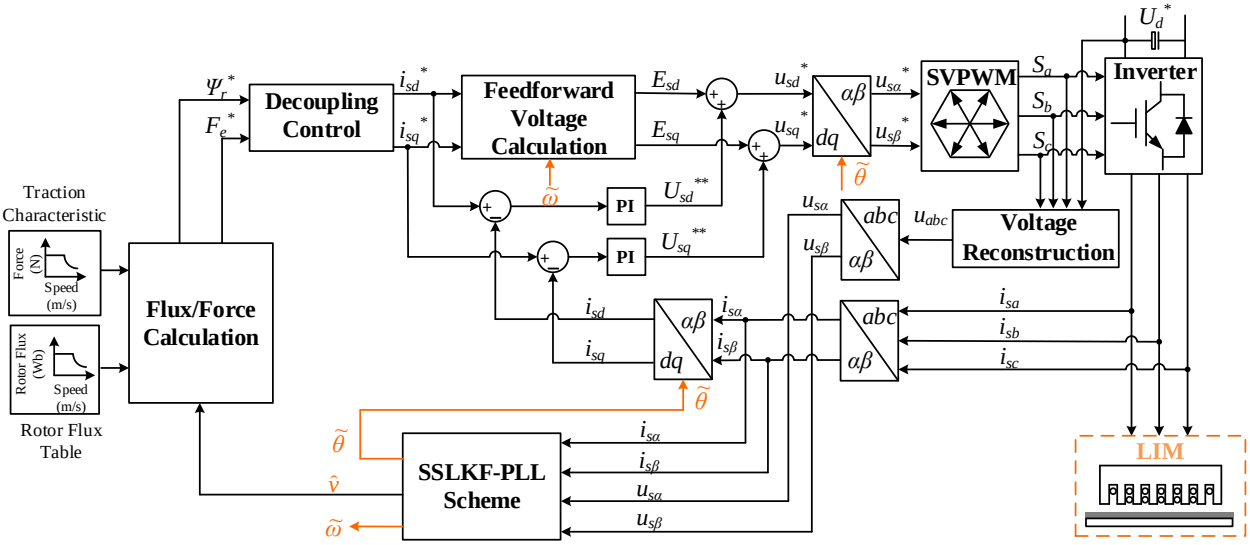


Fig. 13. Block diagram of the entire speed-sensorless drive system (SVPWM-Space vector pulse-width modulation).

Moreover, the performance of thrust force and phase-A current is also provided, which can be found in Fig. 20. As shown in Fig. 20, the thrust force and phase-A current work well during the acceleration process. Notably, the ripples in the thrust force and the distortions in the phase-A current are also observed, which are caused by the low switching frequency.

In Fig. 21, the SSLKF-PLL scheme is operated in the case of load variations. In this case, the load changes from 1000 N to 1800 N, and then back to 1300 N. As a result, the estimated speed tracks the actual speed well under the load variations. Moreover, due to the effect of the low switching frequency, there are some ripples in the thrust force and obvious distortions in the phase-A current.

As mentioned previously, the model-based speed estimation schemes are sensitive to parameter variations. Therefore, the effectiveness of the SSLKF-PLL scheme in addressing the issue of stator resistance variations is also verified. The experimental results are shown in Fig. 22 (notice that $R_s$ denotes the stator resistance in Fig. 22). It is known that with the assistance of the AN unit, the SSLKF-PLL scheme still achieves acceptable speed estimation performance in the case of stator resistance variations.

### *D. Disturbance Rejection Performance*

As discussed previously, the performance of the rotor back EMFs is of importance in the SSLKF-PLL scheme, and it is guaranteed by employing the pre-filters and the AN unit. To verify the discussions, further experimental tests are performed. Fig. 23 presents the performance comparison of the rotor back EMFs with and without the pre-filters. As shown in Fig. 23(a), severe distortions have been seen in the rotor back EMFs without the pre-filters, and accordingly, the harmonics in the rotor back EMFs result in the obvious oscillations in the estimated parameters. This will then ruin the speed estimation accuracy, as analyzed previously. In contrast, as observed in Fig. 23(b), the pre-filters can effectively improve the performance of the rotor back EMFs. Consequently, the speed estimation of the SSLKF-PLL scheme can be maintained.

Furthermore, the effect of the AN unit is explored, and the results are presented in Figs. 24 and 25. It can be seen in Figs. 24 and 25 that the rotor back EMFs behave well after the the stator resistance variations, when the AN unit is executed. As a result, the speed estimation performance of the SSLKF-PLL scheme is guaranteed under stator resistance variations.

## VI. Conclusion

This paper presented a speed estimation scheme based on the SSLKF-PLL system for speed-sensorless control of LIM drives. Before the introduction of the SSLKF-PLL scheme, the model of the SSLKF-PLL system was detailed. Then, the speed estimation scheme was implemented based on the SSLKF-PLL system. Considering the SSLKF-PLL scheme has a limited capability to deal with the issues of harmonics and parameter variations in practice, the disturbance rejection schemes consisting of the pre-filters and an AN unit were employed in the SSLKF-PLL scheme to maintain speed estimation. Moreover, the dynamic performance analysis of the SSLKF-PLL scheme has been elaborated to reveal that the SSLKF-PLL scheme can track frequency ramps accurately. Additionally, the parameter tuning of the SSLKF-PLL scheme has been presented in this paper. The experimental tests have verified the effectiveness of the SSLKF-PLL scheme.

## Appendix

### Model of the SSLKF-PLL system in the *s*-Domain

According to the block diagram of the SSLKF-PLL system in Fig. 1(a), it can be given as

$$\begin{cases} \hat{a}(\lambda) = k_3 v_q(\lambda) + \hat{a}(\lambda - 1) \\ \tilde{\omega}(\lambda) = \hat{a}(\lambda - 1) T_s + \hat{\omega}(\lambda - 1) \\ \hat{\omega}(\lambda) = k_2 v_q(\lambda) + \tilde{\omega}(\lambda) \end{cases} \quad \text{(A-1)}$$

where $T_s$ and $\lambda$ are the sampling time and the sampling instant. Subsequently,

$$\begin{cases} \hat{a}(\lambda) = \dfrac{k_3 v_q(\lambda)}{1-z^{-1}} \\ \tilde{\omega}(\lambda) = \hat{a}(\lambda-1)T_s + \hat{\omega}(\lambda-1) \\ \qquad = \dfrac{k_3 v_q(\lambda)}{1-z^{-1}} z^{-1}T_s + [k_2 v_q(\lambda) + \tilde{\omega}(\lambda)]z^{-1} \end{cases} \tag{A-2}$$

Based on (A-2), it can be given as

$$\begin{aligned} \tilde{\omega}(\lambda) &= \frac{1}{1-z^{-1}}\left[\hat{a}(\lambda-1)T_s + k_2 v_q(\lambda)z^{-1}\right] \\ &= \frac{1}{1-z^{-1}}[\frac{k_3 v_q(\lambda)}{1-z^{-1}} z^{-1}T_s + k_2 v_q(\lambda)z^{-1}] \\ &= \frac{z}{z-1}[\frac{k_3 v_q(\lambda)}{z-1} T_s + k_2 v_q(\lambda)z^{-1}] \end{aligned} \tag{A-3}$$

Assuming that $k_3' = k_3/T_s$ and $k_2' = k_2/T_s$, and substituting them into (A-3) yields

$$\begin{aligned} \tilde{\omega}(\lambda) &= \hat{a}(\lambda-1)T_s + \hat{\omega}(\lambda-1) \\ &= \frac{T_s}{z-1}\{\underbrace{\frac{zT_s}{z-1}[k_3' v_q(\lambda)]}_{H_1(z)} + \underbrace{k_2' v_q(\lambda)}_{H_2(z)}\} \end{aligned} \tag{A-4}$$

Similarly, it can be obtained as

$$\begin{cases} \tilde{\theta}(\lambda) = \hat{a}(\lambda)z^{-1}T_s^2/2 + \hat{\omega}(\lambda)z^{-1}T_s + \hat{\theta}(\lambda)z^{-1} \\ \hat{\theta}(\lambda) = k_1 v_q(\lambda) + \tilde{\theta}(\lambda) \\ \hat{\omega}(\lambda)z^{-1} = \tilde{\omega}(\lambda) - \hat{a}(\lambda)z^{-1}T_s \end{cases} \tag{A-5}$$

Subsequently,

$$\begin{aligned} \tilde{\theta}(\lambda) &= \hat{a}(\lambda)z^{-1}\frac{T_s^2}{2} + \hat{\omega}(\lambda)z^{-1}T_s + \hat{\theta}(\lambda)z^{-1} \\ &= \hat{a}(\lambda)z^{-1}\frac{T_s^2}{2} + [\tilde{\omega}(\lambda) - \hat{a}(\lambda)z^{-1}T_s]T_s + [k_1 v_q(\lambda) + \tilde{\theta}(\lambda)]z^{-1} \end{aligned} \tag{A-6}$$

Then, it can be obtained that

$$\begin{aligned} \tilde{\theta}(\lambda) &= \frac{1}{(1-z^{-1})}[-\hat{a}(\lambda)z^{-1}T_s^2/2 + \tilde{\omega}(\lambda)T_s + k_1 v_q(\lambda)z^{-1}] \\ &= -\frac{1}{z-1}(\frac{k_3 v_q(\lambda)}{1-z^{-1}})T_s^2/2 + \frac{zT_s}{z-1}\tilde{\omega}(\lambda) + \frac{T_s}{z-1}k_1' v_q(\lambda) \\ &= \frac{zT_s}{z-1}\left[\frac{T_s}{z-1}\left(-\frac{T_s}{2}k_3' v_q(\lambda)\right)\right] + \frac{zT_s}{z-1}\left[\tilde{\omega}(\lambda)\right] + \frac{T_s}{z-1}\left[k_1' v_q(\lambda)\right] \\ &= \frac{T_s}{z-1}\{\left[\frac{zT_s}{z-1}\left(-\frac{T_s}{2}k_3' v_q(\lambda)\right)\right] + \left[z\tilde{\omega}(\lambda)\right] + \left[k_1' v_q(\lambda)\right]\} \end{aligned} \tag{A-7}$$

where $k_1' = k_1/T_s$. Substituting (A-4) into (A-7) yields

$$\begin{aligned} \tilde{\theta}(\lambda) &= \frac{T_s}{z-1}\{\left[\frac{zT_s}{z-1}\left(-\frac{T_s}{2}k_3' v_q(\lambda)\right)\right] + \left[z\tilde{\omega}(\lambda)\right] + \left[k_1' v_q(\lambda)\right]\} \\ &= \frac{T_s}{z-1}\{\underbrace{\left[\frac{zT_s}{z-1}\left(-\frac{T_s}{2}k_3' v_q(\lambda)\right)\right]}_{F_1(z)} \\ &\quad + \underbrace{\frac{zT_s}{z-1}\{\underbrace{\frac{zT_s}{z-1}[k_3' v_q(\lambda)]}_{H_1(z)} + \underbrace{k_2' v_q(\lambda)}_{H_2(z)}\}}_{F_2(z)} + \underbrace{\left[k_1' v_q(\lambda)\right]}_{F_3(z)}\} \end{aligned} \tag{A-8}$$

Based on (A-8), the block diagram of the SSLKF-PLL system in the *z*-domain can be presented in an alternative way, which can be found in Fig. A1. Notice that, in this structure, $\frac{zT_s}{z-1}$ and $\frac{T_s}{z-1}$ describe two discretized integrators using the backward and forward Euler methods, respectively. Accordingly, the block diagram of the SSLKF-PLL system in the *s*-domain is depicted in Fig. 1(b).

## REFERENCES


[1] J. H. Jeong, C. W. Ha, J. Lim, and J. Y. Choi, "Analysis and control of electromagnetic coupling effect of levitation and guidance systems for semi-high-speed maglev train considering current direction," *IEEE Trans. Magn.*, vol. 53, no. 6, pp. 1-4, Jun. 2017.

[2] H. Lee, K. Kim, and J. Lee, "Review of maglev train technologies," *IEEE Trans. Magn.*, vol. 42, no. 7, pp. 1917-1925, Jul. 2006.

[3] N. Prasad, S. Jain, and S. Gupta, "Electrical components of maglev systems: Emerging trends," *Urban Rail Transit*, vol. 5, no. 2, pp. 67-79, May 2019.

[4] J. Holtz, "Sensorless control of induction motor drives," *Proc. IEEE*, vol. 90, no. 8, pp. 1359-1394, Aug. 2002.

[5] M. Cirrincione, A. Accetta, M. Pucci, and G. Vitale, "MRAS speed observer for high-performance linear induction motor drives based on linear neural networks," *IEEE Trans. Power Electron.*, vol. 28, no. 1, pp. 123-134, Jan. 2012.

[6] A. Accetta, M. Cirrincione, M. Pucci, and G. Vitale, "Neural sensorless control of linear induction motors by a full-order Luenberger observer considering the end effects," *IEEE Trans. Ind. Appl.*, vol. 50, no. 3, pp. 1891-1904, May/Jun. 2014.

[7] F. Alonge, M. Cirrincione, F. D'Ippolito, M. Pucci, A. Sferlazza, and G. Vitale, "Descriptor-type Kalman filter and TLS EXIN speed estimate for sensorless control of a linear induction motor," *IEEE Trans. Ind. Appl.*, vol. 50, no. 6, pp. 3754-3766, Nov./Dec. 2014.

[8] A. Accetta, M. Cirrincione, M. Pucci, and G. Vitale, "Closed-loop MRAS speed observer for linear induction motor drives," *IEEE Trans. Ind. Appl.*, vol. 51, no. 3, pp. 2279-2290, May/Jun. 2015.

[9] H. Wang, X. Ge, and Y. C. Liu, "Second-order sliding-mode MRAS observer based sensorless vector control of linear induction motor drives for medium-low speed maglev applications," *IEEE Trans. Ind. Electron.*, vol. 65, no. 12, pp. 9938-9952, Dec. 2018.

[10] P. Liu, C. Y. Hung, C. S. Chiu, and K. Y. Lian, "Sensorless linear induction motor speed tracking using fuzzy observers," *IET Elect. Power Appl.*, vol. 5, no. 4, pp. 325-334, Jul. 2011.

[11] C. Y. Hung, P. Liu, and K. Y. Lian, "Fuzzy virtual reference model sensorless tracking control for linear induction motors," *IEEE Trans. Cybern.*, vol. 43, no. 3, pp. 970-981, Jun. 2013.

[12] J. Thomas and A. Hansson, "Speed tracking of a linear induction motor-enumerative nonlinear model predictive control," *IEEE Trans. Control Syst. Technol.*, vol. 21, no. 5, pp. 1956-1962, Sep. 2013.

[13] S. Golestan, J. M. Guerrero, and J. C. Vasquez, "Three-phase PLLs: A review of recent advances," *IEEE Trans. Power Electron.*, vol. 32, no. 3, pp. 1894-1907, Mar. 2017.

This article has been accepted for publication in a future issue of this journal, but has not been fully edited. Content may change prior to final publication. Citation information: DOI 10.1109/TIA.2020.3008673, IEEE Transactions on Industry Applications



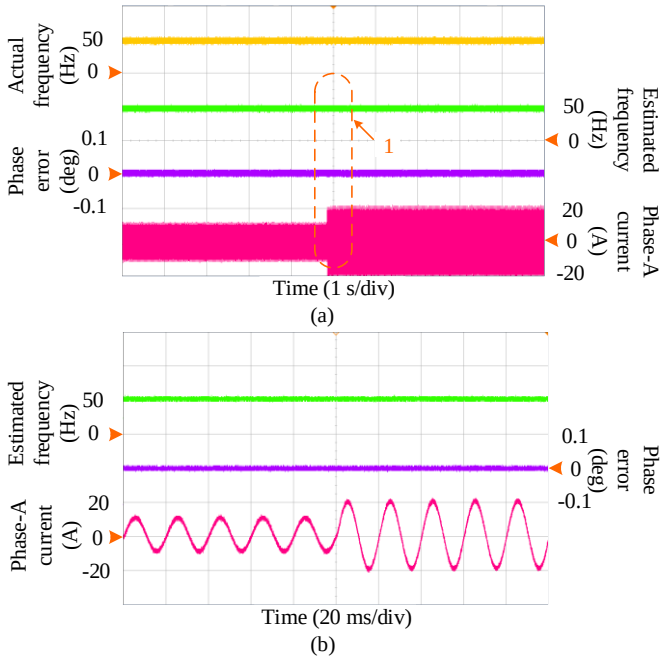


Fig. 14. Dynamic performance of the SSLKF-PLL scheme with the amplitude jump of +10 A: (a) the overall performance and (b) the zoom-in area 1.

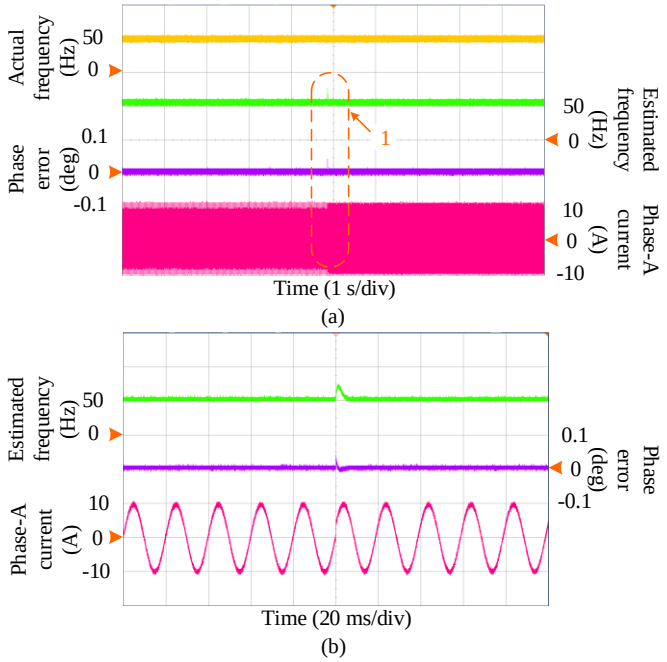


Fig. 15. Dynamic performance of the SSLKF-PLL scheme with the phase jump of +20°: (a) the overall performance and (b) the zoom-in area 1.

[14] S. Golestan, J. M. Guerrero, and J. C. Vasquez, "Single-phase PLLs: A review of recent advances," *IEEE Trans. Power Electron.*, vol. 32, no. 12, pp. 9013-9030, Dec. 2017.

[15] S. Golestan, M. Monfared, F. D. Freijedo, and J. M. Guerrero, "Advantages and challenges of a type-3 PLL," *IEEE Trans. Power Electron*., vol. 28, no. 11, pp. 4985-4997, Nov. 2013.

[16] G. Wang, R. Yang, and D. Xu, "DSP-based control of sensorless IPMSM drives for wide-speed-range operation," *IEEE Trans. Ind. Electron*., vol. 60, no. 2, pp. 720-727, Feb. 2013.

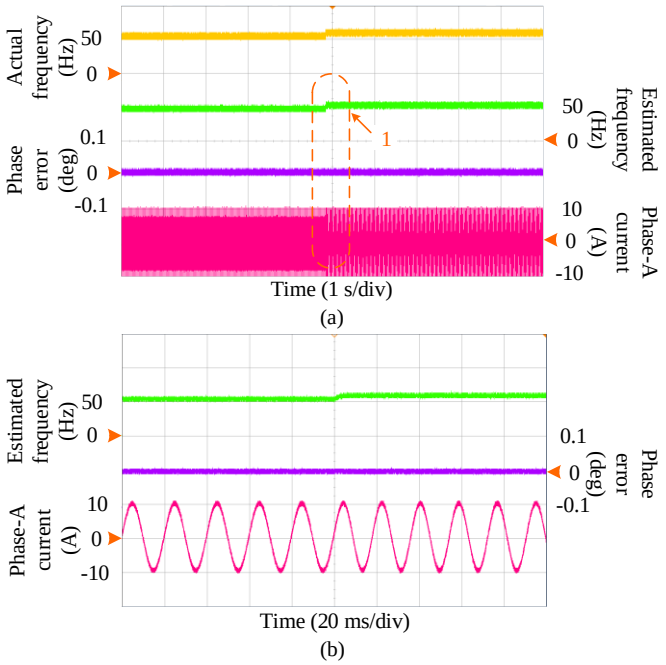


Fig. 16. Dynamic performance of the SSLKF-PLL scheme with the frequency jump of +5 Hz: (a) the overall performance and (b) the zoom-in area 1.

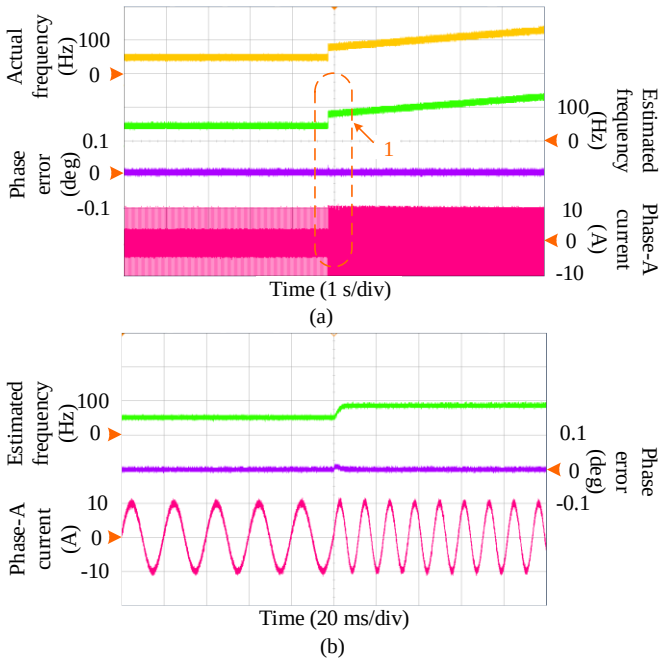


Fig. 17. Dynamic performance of the SSLKF-PLL scheme with the frequency ramp of +10 Hz/s: (a) the overall performance and (b) the zoom-in area 1.

[17] G. Wang, Z. Li, G. Zhang, Y. Yu, and D. Xu, "Quadrature PLL-based high-order sliding-mode observer for IPMSM sensorless control with online MTPA control strategy," *IEEE Trans. Energy Convers*., vol. 28, no. 1, pp. 214-224, Mar. 2013.

[18] G. Wang, T. Li, G. Zhang, X. Gui, and D. Xu, "Position estimation error reduction using recursive-least-square adaptive filter for model based sensorless interior permanent-magnet synchronous motor drives," *IEEE Trans. Ind. Electron.*, vol. 61, no. 9, pp. 5115-5125, Sep. 2014.

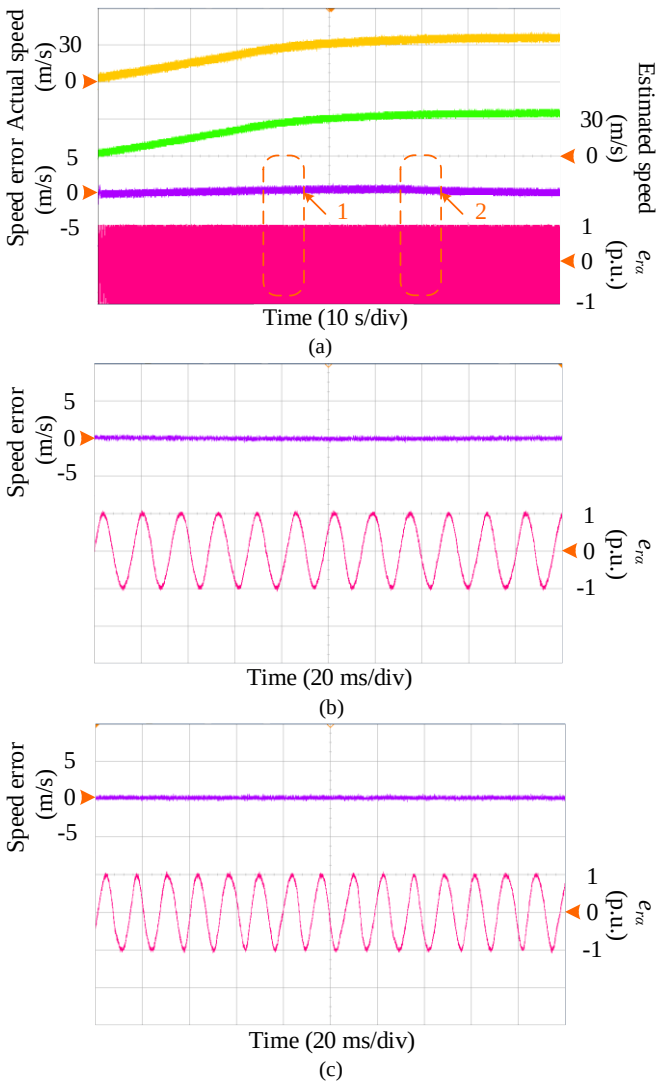


Fig. 18. Speed estimation performance of the SSLKF-PLL scheme in the load of 1000 N: (a) the overall performance, (b) the zoom-in area 1, and (c) the zoom-in area 2.

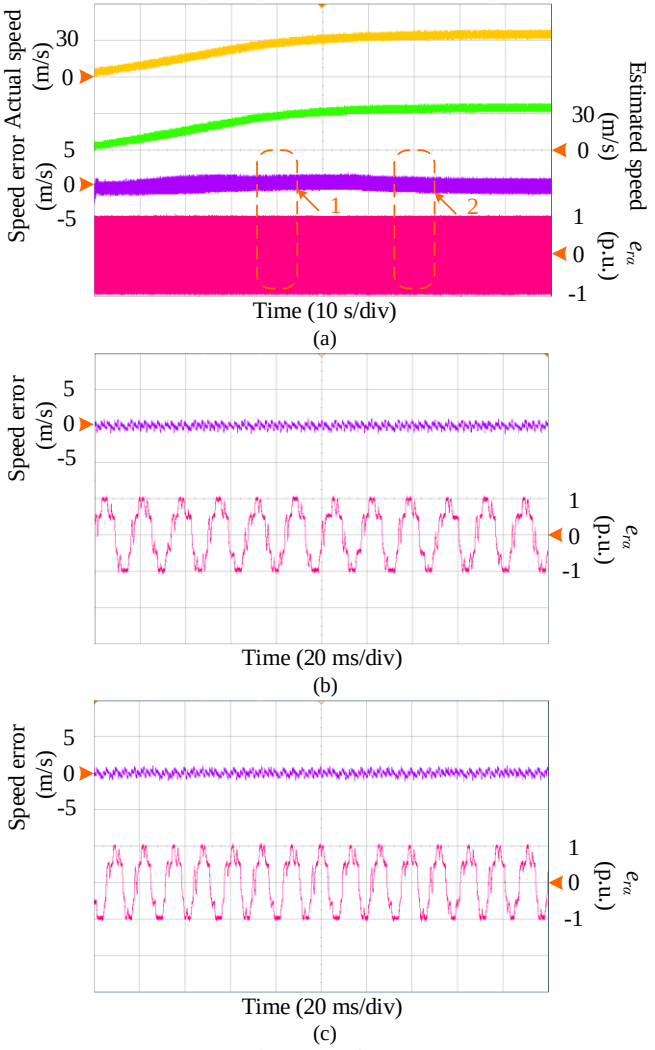


Fig. 19. Speed estimation performance of the SSLKF-PLL scheme without the pre-filters in the load of 1000 N: (a) the overall performance, (b) the zoom-in area 1, and (c) the zoom-in area 2.

[19] G. Wang, H. Zhan, G. Zhang, X. Gui, and D. Xu, "Adaptive compensation method of position estimation harmonic error for EMF-based observer in sensorless IPMSM drives," *IEEE Trans. Power Electron*., vol. 29, no. 6, pp. 3055-3064, Jun. 2014.

[20] G. Zhang, G. Wang, D. Xu, and N. Zhao, "ADALINE-network-based PLL for position sensorless interior permanent magnet synchronous motor drives," *IEEE Trans. Power Electron*., vol. 31, no. 2, pp. 1450-1460, Feb. 2016.

[21] G. Zhang, G. Wang, D. Xu, R. Ni, and C. Jia, "Multiple-AVF cross-feedback-network-based position error harmonic fluctuation elimination for sensorless IPMSM drives," *IEEE Trans. Ind. Electron*., vol. 63, no. 2, pp. 821-831, Feb. 2016.

[22] M. Abdelrahem, C. M. Hackl, and R. Kennel. "Finite position set-phase locked loop for sensorless control of direct-driven permanent-magnet synchronous generators," *IEEE Trans. Power Electron.*, vol. 33, no. 4, pp. 3097-3105, Apr. 2018.

[23] M. H. Bierhoff, "A general PLL-type algorithm for speed sensorless control of electrical drives," *IEEE Trans. Ind. Electron*., vol. 64, no. 12, pp. 9253-9260, Apr. 2017.

[24] A. Srivorakul and S. Suwankawin, "A synchro-perspective-based high-frequency voltage injection method for position-sensorless vector control of doubly fed induction machines," *IEEE Trans. Ind. Appl*., vol. 54, no. 4, pp. 3326-337, Jul./Aug. 2018.

[25] H. X. Nguyen, T. N. C. Tran, J. W. Park, and J. W. Jeon, "An adaptive linear neuron based third-order PLL to improve the accuracy of absolute magnetic encoders," *IEEE Trans. Ind. Electron.*, vol. 66, no. 6, pp. 4639-4649, Jun. 2019.

[26] H. Wang and X. Ge, "Type-3 PLL based speed estimation scheme for sensorless linear induction motor drives," in *Proc. IEEE Conf. Power Electron. (ICPE 2019-ECCE-Asia)*, pp. 1303-1308, May 2019.

[27] H. A. Hamed and M. S. E. Moursi, "A new type-2 PLL based on unit delay phase angle error compensation during the frequency ramp," *IEEE Trans. Power Syst.*, vol. 34, no. 4, pp. 3289-3293, Jul. 2019.

[28] H. Wang, X. Ge, Y. Yue, and Y. Liu, "Dual phase-locked loop based speed estimation scheme for sensorless vector control of linear induction motor drives," *IEEE Trans. Ind. Electron*., vol. 67, no. 7, pp. 5900-5912, Jul. 2020.

[29] H. Machida, M. Kambara, K. Tanaka, and F. Kobayashi, "A motor speed control system using a hybrid of dual-loop PLL and feed-forward," in *Proc. Int. Workshop Adv. Motion Control AMC*, pp. 185-190, Mar. 2010.

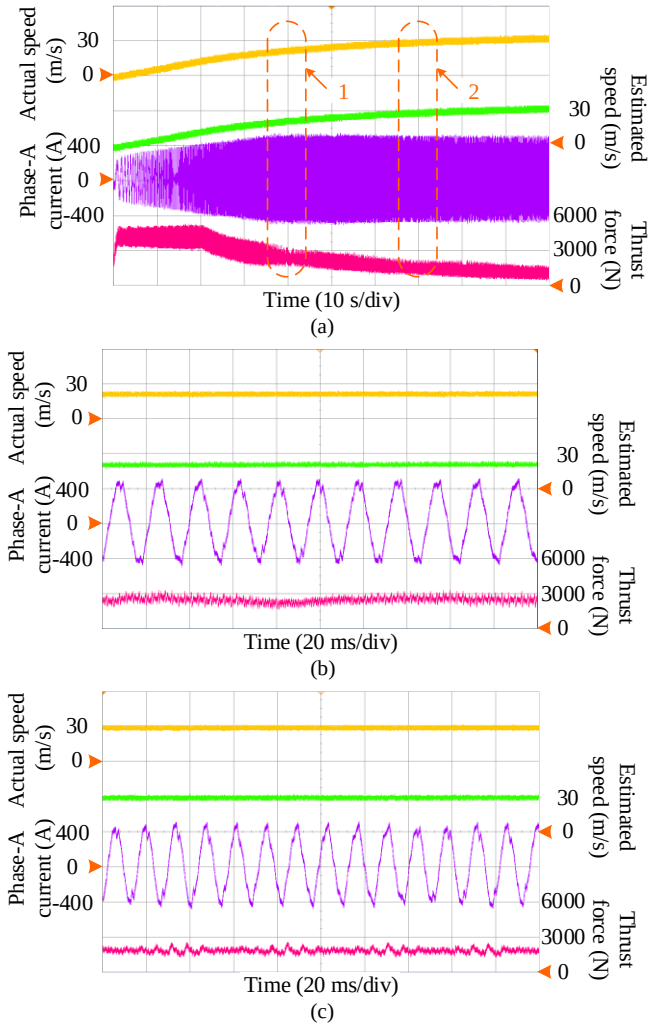


Fig. 20. Performance of speed estimation in the load of 1000 N: (a) the overall performance, (b) the zoom-in area 1, and (c) the zoom-in area 2.

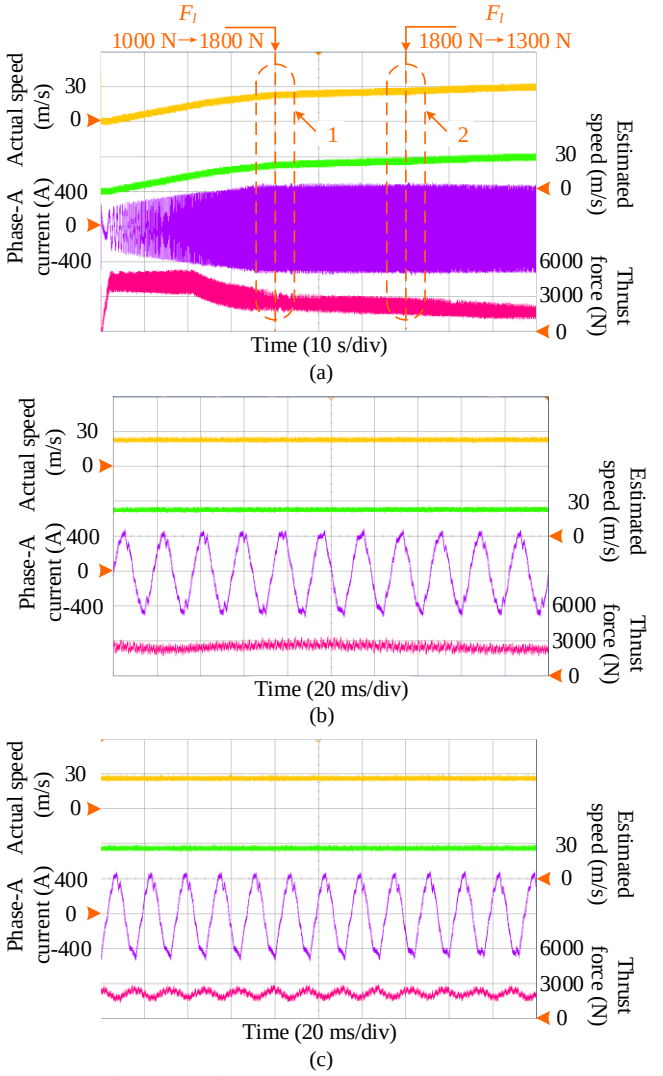


Fig. 21. Performance of speed estimation in the load variations: (a) the overall performance, (b) the zoom-in area 1, and (c) the zoom-in area 2.


[30] T. N. Tran, H. X. Nguyen, J. W. Park, and J. W. Jeon, "Improving the accuracy of an absolute magnetic encoder by using harmonic rejection and a dual phase-locked loop," *IEEE Trans. Ind. Electron.*, vol. 66, no. 7, pp. 5476-5486, Jul. 2019.

[31] H. Wang, S. Li, Y. Zuo, and X. Ge, "Sensorless control of linear induction motor based on SSLKF-PLL speed estimation scheme," in *Proc. Conf. Electric. Machine Syst.* (*ICEMS 2019*), pp. 1-6, Aug. 2019.

[32] S. Bifaretti, P. Zanchetta, and E. Lavopa, "Comparison of two three-phase PLL systems for more electric aircraft converters," *IEEE Trans. Power Electron.*, vol. 29, no. 12, pp. 6810-6820, Dec. 2014.

[33] A. Bellini, S. Bifaretti, and F. Giannini, "A robust synchronization method for centralized microgrids," *IEEE Trans. Ind. Appl.*, vol. 51, no. 2, pp. 1602-1609, Mar./Apr. 2015.

[34] S. Bifaretti, A. Lidozzi, L. Solero, and F. Crescimbini, "Anti-islanding detector based on a robust PLL," *IEEE Trans. Ind. Appl.*, vol. 51, no. 1, pp. 398-405, Jan./Feb. 2015.

[35] S. Golestan, J. M. Guerrero, and J. C. Vasquez, "Steady-state linear Kalman filter-based PLLs for power applications: A second look," *IEEE Trans. Ind. Electron.*, vol. 65, no. 12, pp. 9795-9800, Dec. 2018.

[36] M. S. Zaky, M. M. Khater, S. S. Shokralla, and H. A. Yasin, "Wide-speed-range estimation with online parameter identification schemes of sensorless induction motor drives," *IEEE Trans. Ind. Electron.*, vol. 56, no. 5, pp. 1699-1707, May 2009.

[37] L. Zhao, J. Huang, H. Liu, B. Li, and W. Kong, "Second-order sliding-mode observer with online parameter identification for sensorless induction motor drives," *IEEE Trans. Ind. Electron.*, vol. 61, no. 10, pp. 5280-5289, Oct. 2014.

[38] J. Chen, J. Huang, and Y. Sun, "Resistances and speed estimation in sensorless induction motor drives using a model with known regressors," *IEEE Trans. Industrial Electron.*, vol. 66, no. 4, pp. 2659-2667, Apr. 2019.

[39] D. Liang, J. Li, and R. Qu, "Sensorless control of permanent magnet synchronous machine based on second-order sliding-mode observer with online resistance estimation," *IEEE Trans. Ind. Appl.*, vol. 53, no. 4, pp. 3672-3682, Jul./Aug. 2017.

[40] S. Golestan, M. Monfared, F. D. Freijedo, and J. M. Guerrero, "Performance improvement of a prefiltered synchronous-reference-frame PLL by using a PID-type loop filter," *IEEE Trans. Ind. Electron.*, vol. 61, no. 7, pp. 3469-3479, Jul. 2014.

[41] F. D. Freijedo, J. D. Gandoy, O. Lopez, and E. Acha, "Tuning of phase-locked loops for power converters under distorted utility conditions," *IEEE Trans. Ind. Appl.*, vol. 45, no. 9, pp. 2039-2047, Nov./Dec. 2009.

[42] S. Golestan, F. D. Freijedo, and J. M. Guerrero, "A systematic approach to design high-order phase-locked loops," *IEEE Trans. Power Electron.*, vol. 30, no. 6, pp. 2885-2890, Jun. 2015.

[43] P. Lin, T. Zhao, B. Wang, Y. Wang, and P. Wang, "A semi-consensus strategy toward multi-functional hybrid energy storage system in DC microgrids," *IEEE Trans. Energy Convers.*, vol. 35, no. 1, pp. 336-346, Mar. 2020.

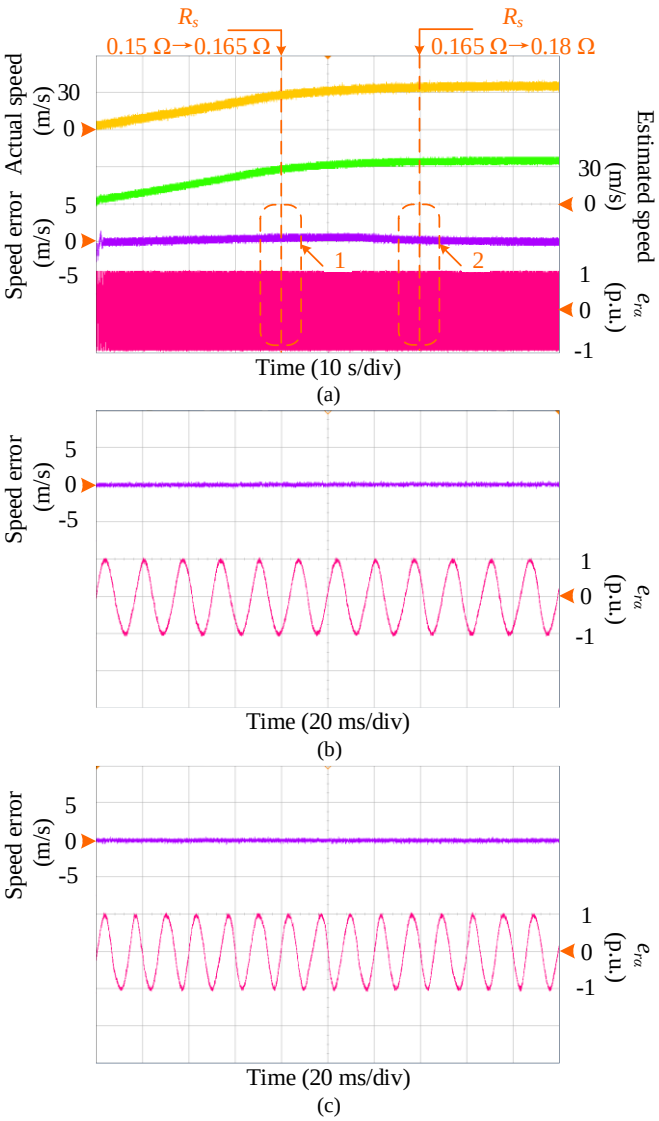


Fig. 22. Speed estimation performance of the SSLKF-PLL scheme in the step increases of stator resistance: (a) the overall performance, (b) the zoom-in area 1, and (c) the zoom-in area 2.

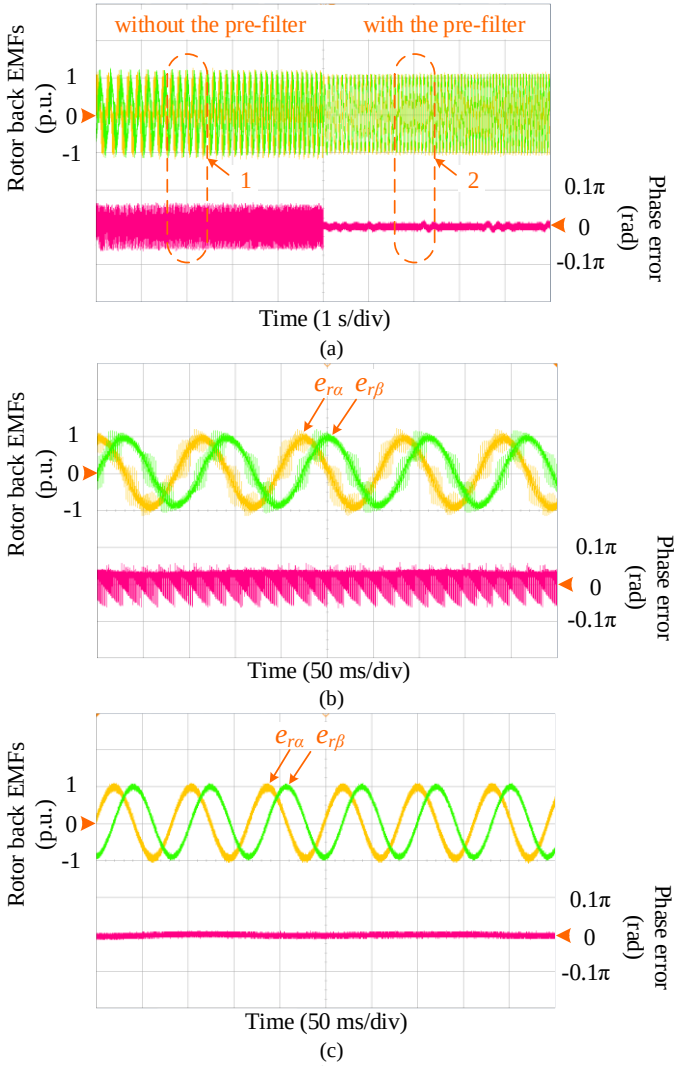


Fig. 23. Experimental test results of the rotor back EMFs: (a) the overall performance comparison, (b) without the pre-filters, and (c) with the pre-filters.

This article has been accepted for publication in a future issue of this journal, but has not been fully edited. Content may change prior to final publication. Citation information: DOI 10.1109/TIA.2020.3008673, IEEE Transactions on Industry Applications



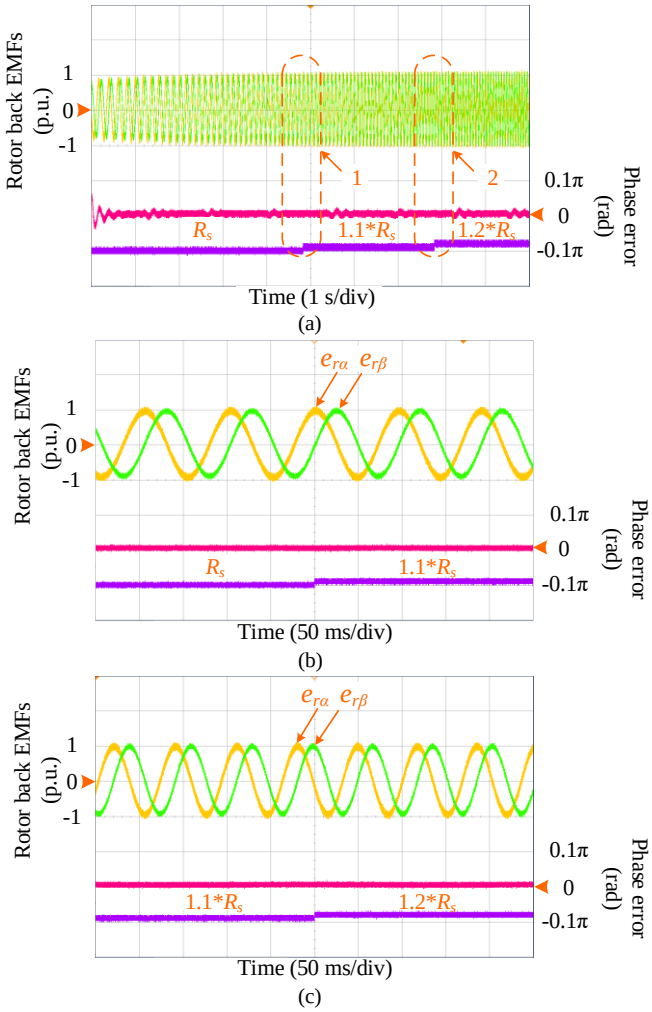


Fig. 24. Experimental test results of the rotor back EMFs in the step increases of stator resistance: (a) the overall performance of the rotor back EMFs, (b) the zoom-in area 1, and (c) the zoom-in area 2.

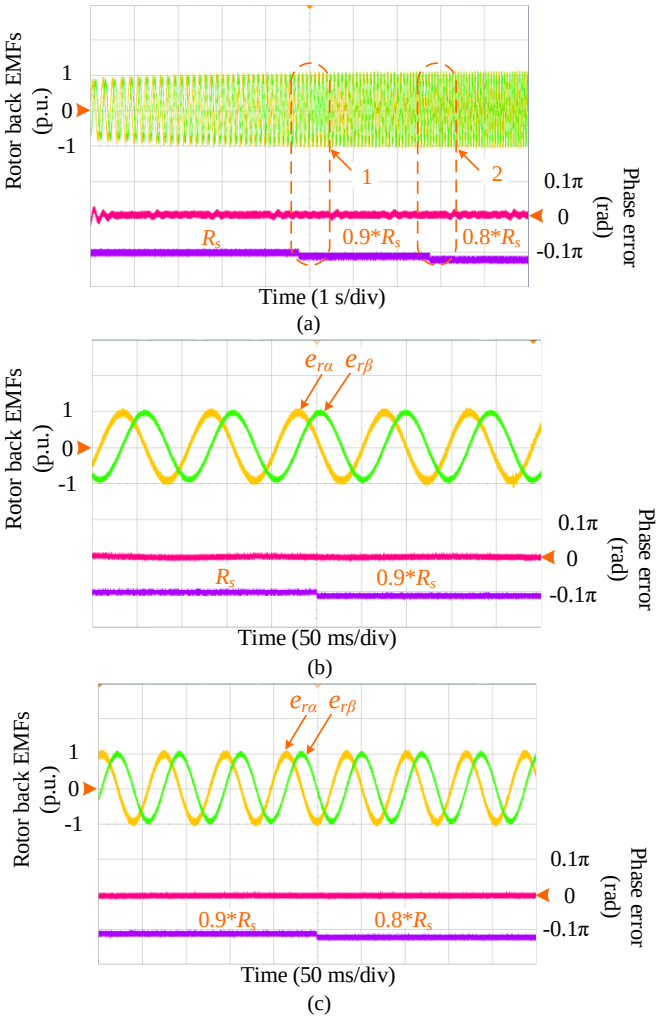


Fig. 25. Experimental test results of the rotor back EMFs in the step decreases of stator resistance: (a) the overall performance of the rotor back EMFs, (b) the zoom-in area 1, and (c) the zoom-in area 2.

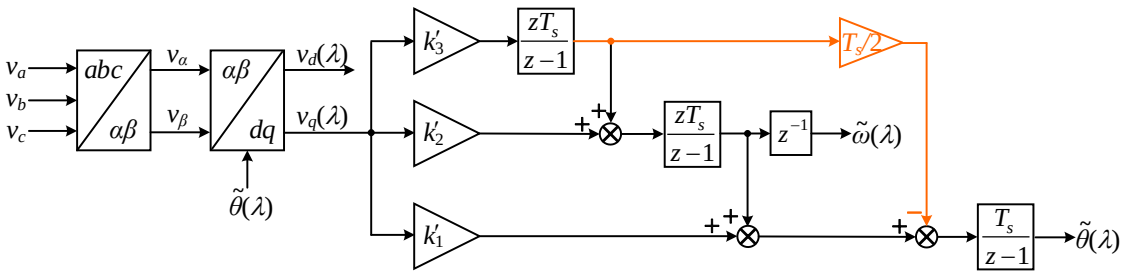


Fig. A1. Alternative representation of the SSLKF-PLL system in the *z*-domain.

**Huimin Wang** (S'17) received the B.Eng. degrees in electrical engineering from Southwest Jiaotong University (SWJTU), Chengdu, China, in 2016. He is currently working toward the Ph.D. degree in electrical engineering at the Southwest Jiaotong University, Chengdu, China.

His research interests include induction motor drive system and its speed-sensorless control, and synchronization technique in grid-connected system.

Mr. Wang was a recipient of the Best Paper Award of IEEE Transportation Electrification Conference and EXPO Asia-Pacific (ITEC Asia-Pacific) in 2019.

**Yongheng Yang** (SM'17) received the B.Eng. degree in electrical engineering and automation from Northwestern Polytechnical University, Shaanxi, China, in 2009 and the Ph.D. degree in electrical engineering from Aalborg University, Aalborg, Denmark, in 2014.

He was a postgraduate student with Southeast University, China, from 2009 to 2011. In 2013, he spent three months as a Visiting Scholar at Texas A&M University, USA. Currently, he is an Associate Professor with the Department of Energy Technology, Aalborg University, where he also serves as the Vice Program Leader for the research program on photovoltaic systems. His current research is on the integration of grid-friendly photovoltaic systems with an emphasis on the power electronics converter design, control, and reliability.

Dr. Yang is the Chair of the IEEE Denmark Section. He serves as an Associate Editor for several prestigious journals, including the IEEE TRANSACTIONS ON INDUSTRIAL ELECTRONICS, the IEEE TRANSACTIONS ON POWER ELECTRONICS, and the IEEE Industry Applications Society (IAS) Publications. He is a Subject Editor of the *IET Renewable Power Generation* for Solar Photovoltaic Systems, including the Maximum Power Point Tracking. He was the recipient of the 2018 *IET Renewable Power Generation* Premium Award and was an Outstanding Reviewer for the IEEE TRANSACTIONS ON POWER ELECTRONICS in 2018.

**Xinglai Ge** (M'15) received the B.S., M.S., and Ph.D. degrees in electrical engineering from Southwest Jiaotong University (SWJTU), Chengdu, China, in 2001, 2004, and 2010, respectively. He is currently a Full Professor in the School of Electrical Engineering, Southwest Jiaotong University and a Vice Director of Department of Power Electronics and Power Drive.

From July to August of 2012, he was a visiting scholar at George Mason University, VA, USA. From October 2013 to October 2014, he was a visiting scholar at the School of Electrical and Computer Engineering, Georgia Institute of Technology, Atlanta, GA, USA. He is the author and co-author of more than 60 technical papers

His research interests include stability analysis and control of electrical traction system, fault diagnosis and hardware-in-the-loop simulation of traction converter and motor drive system.

**Songtao Li** received the B.Eng. degree in electrical engineering from the Lanzhou University of Technology, Lanzhou, China, in 2018. He is currently pursuing the M.Eng. degree in power electronics and electrical drives with the School of Electrical Engineering, Southwest Jiaotong University, Chengdu, China.

His current research interests include permanent magnet synchronous motor drives and position sensorless control.

**Zuo Yun** received the B.Eng. degree in electrical engineering and automation from Dalian Jiaotong University, Dalian, China, in 2019. He is currently pursuing the M.Eng. degree in electrical engineering with Southwest Jiaotong University, Chengdu, China.

His research interests include induction motor drive systems and its speed-sensorless control.